Coexisting Phases in $NaNbO_3$ Thin Films Influenced by Epitaxial Strain and Size Effects

Aarushi Khandelwal, Kevin J. Crust, Reza Ghanbari, Yijun Yu, Ruijuan Xu*, and Harold Y. Hwang*

Aarushi Khandelwal, Kevin, J. Crust, Yijun Yu, Prof. Harold Y. Hwang
Stanford Institute for Materials and Energy Sciences
SLAC National Accelerator Laboratory
Menlo Park, CA, 94025 USA
E-mail: kcrust@stanford.edu

Aarushi Khandelwal, Yijun Yu, Prof. Harold Y. Hwang
Department of Applied Physics
Stanford University
Stanford, CA, 94305, USA

Kevin J. Crust
Department of Physics
Stanford University
Stanford, CA, 94305, USA

Reza Ghanbari, Prof. Ruijuan Xu
Department of Materials Science and Engineering
North Carolina State University
Raleigh, NC, 27606, USA
Email: rxu22@ncsu.edu

Funding: Work at SLAC/Stanford was supported by the U.S. DOE, Office of Basic Energy Sciences, Division of Materials Sciences and Engineering, under Contract No. DE-AC02-76SF00515. Part of this work was performed at the Stanford Nano Shared Facilities (SNSF) RRID:SCR_023230, supported by the National Science Foundation under award ECCS-2026822. R.G. and R.X. acknowledge the support from the National Science Foundation

(NSF) under award No. DMR-2442399 and the American Chemical Society Petroleum Research Fund under award No. 68244-DNI10.

Keywords: sodium niobate, antiferroelectrics, dielectric capacitors, phase coexistence, size effects

Antiferroelectrics are a promising class of materials for applications in capacitive energy storage and multi-state memory, but comprehensive control of their functional properties requires further research. In thin films, epitaxial strain and size effects are important tuning knobs but difficult to probe simultaneously due to low critical thicknesses of common lead-based antiferroelectrics. Antiferroelectric $NaNbO_3$ enables opportunities for studying size effects under strain but electrical properties of ultra-thin films have not been thoroughly investigated due to materials challenges. Here, high-quality, epitaxial, coherently-strained $NaNbO_3$ films are synthesized from 35- to 250- nm thickness, revealing a transition from a fully ferroelectric state to coexisting ferroelectric and antiferroelectric phases with increasing thickness. The electrical performance of this phase coexistence is analyzed through positive-up negative-down and first-order reversal curve measurements. Further increasing thickness leads to a fully ferroelectric state due to a strain relief mechanism that suppresses the antiferroelectricity. The potential of engineering competing ferroic orders in $NaNbO_3$ for multiple applications is evaluated, reporting significantly enhanced recoverable energy density (20.6 J cm^{-3} at 35 nm) and energy efficiency (90% at 150 nm) relative to pure bulk $NaNbO_3$ as well as strong retention and fatigue performance with multiple accessible polarization states in the intermediate thickness films.

Aarushi Khandelwal and Kevin J. Crust contributed equally to this work.

1. Introduction

Antiferroelectric (AFE) materials, which possess antiparallel electric dipoles that can be reoriented into a parallel ferroelectric (FE) state under a sufficiently strong electric field, are a promising class of materials for applications like capacitive energy storage, multistate random access memory, actuation, and electrocaloric cooling due to the large structural and property changes that occur during the dipole reorientation process.[1–3] Although a theoretical framework for antiferroelectricity was established in 1951,[4] a complete understanding of its underlying mechanisms and control of its functional properties remains lacking. This is particularly true in thin films, which offer significant engineering opportunities and can manifest drastically different behaviors from bulk materials.[1,3] Most AFE thin film studies thus far are of lead-based materials like $PbZrO_3$, which have a significant lattice mismatch from commercially available substrates such as $SrTiO_3$ or $DyScO_3$. Epitaxial strain applied by substrates is an effective knob for tuning the properties of AFE thin films, but the large mismatch leads to relatively low critical thicknesses, typically a few tens of nm, above which the strain is relaxed.[5–7] This both limits the practical applications for which strain engineering can be utilized, as properties like leakage current and coercive field typically perform worse in extremely thin films, and also prevents the study of size effects, another valuable thin film tuning knob, under strain.

$NaNbO_3$ is a promising alternative to the predominant lead-based AFEs, displaying a complex phase diagram with multiple competing ferroic orders stabilized by tuning temperature and applied electric field.[8–11] Bulk $NaNbO_3$ is an AFE material with orthorhombic *Pbcm* space group at room temperature that undergoes an irreversible phase transition to a polar FE phase with orthorhombic $Pmc2_1$ space group under an applied electric field, due to the small energy difference between these phases.[10] Its lattice parameters are also better matched with commercial substrates, allowing thin films to remain coherently strained up to several hundreds of nm in thickness on $SrTiO_3$.[12]

Despite these opportunities, previous studies on strain engineering or size effects in $NaNbO_3$ thin films have been mostly limited to theoretical or structural analyses, with significant questions remaining about the nature of their field-induced transitions. Various FE ground states have been predicted through strain-induced phase transitions, including a monoclinic *Cc* phase with simultaneous in-plane and out-of-plane polarizations for small magnitudes of strain, which is distinct from both the low temperature (*F3c*) or room temperature field-induced ($Pmc2_1$) bulk FE phases.[10,13–16] Strain has been experimentally verified to modify the room temperature ground state of $NaNbO_3$, with a FE ground state

observed in films with large magnitudes of tensile strain, using Raman spectroscopy and piezoresponse force microscopy (PFM), as well as an AFE ground state identified in films with large compressive strain using a superlattice reflection from unit cell quadrupling in the AFE phase.[12,17,18] On $SrTiO_3$, which applies small degree of strain that can either be compressive or tensile depending on the film orientation, both FE and AFE room temperature ground states have been reported.[19–21] Size effects have also been shown to alter the phase balance in the absence of epitaxial strain, with freestanding $NaNbO_3$ membranes transitioning from a single FE phase to coexisting FE and AFE phases with increasing thickness.[22]

Understanding the electrical properties and field-induced transitions in $NaNbO_3$ has been mostly limited to bulk samples due to high leakage currents in thin films. Such leakage has been attributed to point defects in the system, due to sodium vacancies from the highly volatile alkali component or oxygen vacancies akin to other oxide perovskite thin films.[23] This has limited measurements of well-defined polarization – electric field (*P-E)* hysteresis loops for thin films below 200 nm and made it difficult to distinguish between FE and AFE characteristics in electrical characterization of thinner films.[19,24,25] Even for thin films with structurally identified AFE ground states, it is unclear whether they will undergo the same irreversible phase transition as bulk or maintain their AFE character under applied fields, and any influence of size effects on these transitions is currently unknown.

Electrical characterization of $NaNbO_3$ thin films is also essential for determining the potential of $NaNbO_3$ for applications like capacitive energy storage or multistate switching. The main parameters in capacitive energy storage, recoverable energy density and energy efficiency, are directly extracted from *P-E* hysteresis loops by various integrations of the curves and thus optimizing materials towards specific loop shapes is an area of active research.[26] Most work in this direction on bulk $NaNbO_3$-based systems has focused on utilizing chemical substitution to destabilize the FE phase relative to the AFE phase by altering the tolerance factor and polarizability of the B-site cations, but limitations on breakdown fields and energy storage densities persist.[27–30]

On the other hand, multistate switching capabilities, desirable for high density memory and neuromorphic computing applications, are frequently associated with some degree of pinching in *P-E* hysteresis loops and evaluated with pulsed electrical measurements such as positive-up negative-down (PUND) tests to identify stable states with good retention and fatigue tolerance. Several paths have been explored to create these multi-state systems from other bistable ferroelectrics, including controlling switching pathways,[31,32] defect engineering to alter the nucleation processes,[33] or utilizing coexisting structural variants,[34–

[36] with $NaNbO_3$ being a promising candidate for the last pathway given its numerous competing ferroic orders.

In this work, we investigate the impact of size effects under epitaxial strain on $NaNbO_3$ thin films from 35 to 250 nm on $SrTiO_3$ (001) substrates and achieve well-defined *P-E* loops across the entire thickness range via precise control over leakage currents through detailed growth optimization. We observe the coexistence of FE and AFE orders at intermediate thicknesses through detailed electrical and X-ray based structural characterization techniques and reveal a stable intermediate state during electrical switching at these thicknesses. A switching mechanism of this state is proposed and verified through first-order reversal curve (FORC) measurements, including a reversible AFE-FE transition that is not typically observed in bulk $NaNbO_3$. The balance between the coexisting phases is shown to be altered by a mixed-orientation strain relief mechanism which suppresses antiferroelectricity in the thickest film. Finally, we evaluate the application potential of miniaturizing the epitaxially strained $NaNbO_3$ thin films, with decreasing thickness boosting the recoverable energy density in the thinnest film to 20.6 J cm^{-1} and operation in the intermediate state at intermediate thicknesses yielding an energy storage efficiency of 90%, both records for pure $NaNbO_3$. The intermediate state at intermediate thicknesses is also shown to host multiple polarization states with good retention and nearly fatigue-free performance for potential non-volatile memory applications.

2. Results and Discussion

2.1. Structural characterization of $NaNbO_3$ capacitor heterostructures

To investigate the impact of size effects under epitaxial strain on $NaNbO_3$ films, we synthesized $La_{0.7}Sr_{0.3}MnO_3$ / $NaNbO_3$ / $La_{0.7}Sr_{0.3}MnO_3$ tri-layer heterostructures on single-crystalline $SrTiO_3$ (001) substrates by pulsed laser deposition, with the $NaNbO_3$ thickness ranging from 35 to 250 nm. The top $La_{0.7}Sr_{0.3}MnO_3$ layer was etched after photolithographic patterning to create symmetric parallel-plate capacitor structures with 100 μm diameter circular top electrodes (Experimental Section). To mitigate the high leakage currents typically prevalent in $NaNbO_3$, we optimized the growth conditions to minimize leakage while maintaining good crystalline quality of the $NaNbO_3$ films (Figure S1).[19,25,37]

High crystalline quality was confirmed for all samples, evidenced by the 002 θ–2θ X-ray diffraction (XRD) patterns (Figure 1a) that exhibit prominent Laue oscillations in all but the thickest film. The lack of Laue oscillations in the 250 nm film can be attributed to either the resolution limits of our diffractometer or a possible small increase in disorder in the

thickest sample, which could also affect the crystallinity of the top $La_{0.7}Sr_{0.3}MnO_3$ layer. All films display a $NaNbO_3$ film peak at a higher 2θ angle than $SrTiO_3$, corresponding to a lattice parameter between 3.886 Å and 3.894 Å, with the thickest film also exhibiting an additional lower angle peak with a lattice parameter of 3.929 Å. Comparing the reduced pseudocubic cell of bulk $NaNbO_3$ (schematic in Figure 1b,[13,22] $a_{pc} = b_{pc} = 3.915$ Å, $c_{pc} = 3.881$ Å) and the extracted lattice parameters (Figure 1c), we note that the orientation of the $NaNbO_3$ film appears to change with increasing thickness from c_{pc}- oriented to a mixture of structural variants with c_{pc}- and a_{pc} / b_{pc}- orientations.[38] Although bulk lattice parameters of the ferroelectric *Cc* phase are not available, the predicted values are a slight expansion of the *Pbcm* lattice, consistent with our results.[13] Thus, regardless of the FE or AFE phase, the c_{pc}-orientation, with bulk in-plane lattice parameters of ~3.915 Å, experiences biaxial compressive in-plane strain on $SrTiO_3$ substrates. In contrast, the a_{pc} / b_{pc}- orientation, with in-plane lattice parameters of ~3.915 Å and ~3.881 Å, undergoes anisotropic strain – compressive along one in-plane direction and tensile along the other – resulting in a lower compressive strain state. This structural evolution serves as a strain relief mechanism, lowering the increasing strain energy of thicker films through the combined compressive and tensile strains of the mixed c_{pc}- and a_{pc} / b_{pc}- orientations.[12] We also note that the recently reported *Pc* or *Cm* structures could provide an alternative mechanism for this secondary peak in the thickest sample.[16,39]

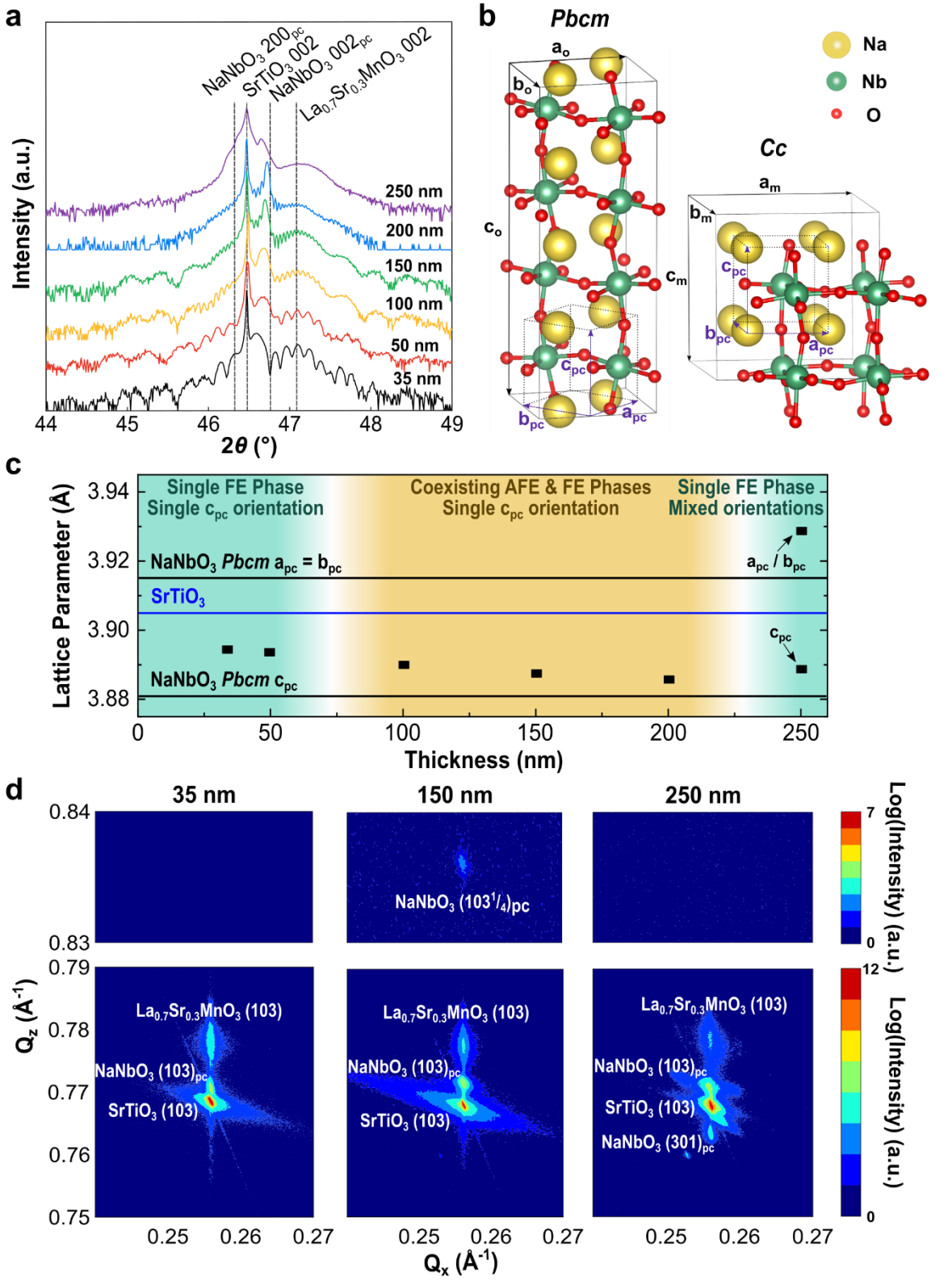

Figure 1. Structural characterization of $La_{0.7}Sr_{0.3}MnO_3$ / $NaNbO_3$ / $La_{0.7}Sr_{0.3}MnO_3$ heterostructures on $SrTiO_3$ (001) substrates. a) X-ray θ–2θ line scans of $La_{0.7}Sr_{0.3}MnO_3$ / $NaNbO_3$ / $La_{0.7}Sr_{0.3}MnO_3$ heterostructures on $SrTiO_3$ (001) substrates with varying $NaNbO_3$ thicknesses. b) Schematic of the antiferroelectric *Pbcm* structure, displaying a quadrupling of the unit cell leading to a quarter-order diffraction peak, and the ferroelectric *Cc* structure,

which only undergoes a doubling of the unit cell. c) Evolution of out-of-plane $NaNbO_3$ lattice parameters with varying film thickness. The solid lines represent the bulk lattice parameters of the room temperature *Pbcm* structure of $NaNbO_3$ as well as $SrTiO_3$. The background is colored based on the thicknesses exhibiting a quarter-order diffraction peak in Figure S2. d) X-ray reciprocal space maps about the (103) diffraction condition for heterostructures with 35, 150, and 250 nm $NaNbO_3$.

We conducted X-ray reciprocal space mapping (RSM) about the $SrTiO_3$ (103) diffraction condition to further understand the $NaNbO_3$ structure and confirmed that all films are coherently epitaxially strained (Figure 1d and Figure S2). Comparing the various thicknesses, an additional $NaNbO_3$ $(301)_{pc}$ peak can be seen only in the 250 nm sample, providing further evidence of the transition to a mixed orientation structure. We also observed the emergence of a quarter-order peak in the intermediate thickness range from 100 to 200 nm. Such a quarter-order diffraction peak is a characteristic feature of the AFE phase in $NaNbO_3$, resulting from the four-fold multiplicity of the *Pbcm* unit cell perpendicular to the polarization direction, whereas the *Cc* structure only undergoes a unit cell doubling (Figure 1b). These results indicate that thinner films only possess FE order, with AFE order appearing as thickness increases, aligned with previous observations in $NaNbO_3$ freestanding membranes.[22] Notably, a splitting of the main $NaNbO_3$ film peak from this phase coexistence could not be observed in either the XRD line scans or RSMs, likely indicating that the phases have similar lattice parameters. As thickness further increases, the AFE phase disappears completely in the 250 nm film. We attribute this to the onset of tensile strain discussed above, which is known to stabilize the FE phase in $NaNbO_3$ and is experienced by the shorter in-plane axis of the a_{pc} / b_{pc}- orientation in the thickest film.[12,17,18]

2.2. Electrical characterization revealing a stable intermediate state during switching

We further study how the thickness-dependent structural evolution and competing AFE and FE phases influence the electrical properties of $NaNbO_3$ films. Although leakage currents typically increase dramatically with reduced thickness,[40] we maintain low leakage currents across the entire thickness range (Figure S3), allowing us to probe well-defined *P-E* loops in all samples. Both the 35 nm and 250 nm films exhibit standard ferroelectric hysteresis loops and similar saturation polarizations (Figure 2a,c and Figure S4 and S5), with the thinner film displaying significantly reduced remnant polarization and more slanted hysteresis loops. This variation between the 35 nm and 250 nm samples can be attributed to

the changes in film orientation with thickness and is directly observable through piezoresponse force microscopy (Figure S6). For the 35 nm samples, the polarization is strongest along the in-plane $[110]_{pc}$ direction with a smaller out-of-plane polarization, providing further evidence for the monoclinic *Cc* phase. In contrast, the 250 nm sample has two laterally segregated regions: a region at lower height with the same predominately in-plane polarization and a region at a higher height with relatively stronger out-of-plane polarization. The difference in height between these regions matches the expected value given the thickness of the film and the difference in out-of-plane lattice parameter between the orientations from Figure 1c.

For the intermediate thickness samples (Figure 2b and Figure S4), we measure pinched hysteresis loops accompanied by multiple peaks in the corresponding switching current curve, which is most evident in the 200 nm sample shown in Figure 2 but still observable at other intermediate thicknesses included in the Supporting Information. The degree of pinching is found to be more pronounced as the frequency decreases (Figure 2d and Figure S5), ruling out defect-induced pinching in these films and instead suggesting that the resultant pinched hysteresis loops are a combination of FE loops and AFE double hysteresis loops, similar to previous work in mixed-phase $NaNbO_3$ systems.[24,29,41] Additionally, while the extracted relative permittivity values ranging between 150 and 200 for the 35 and 250 nm films are similar to previously reported values for $NaNbO_3$,[25,42,43] the intermediate thickness films show a significant increase up to approximately 670 (Figure S7), as expected due to the phase coexistence with multiple ferroic orders.[44]

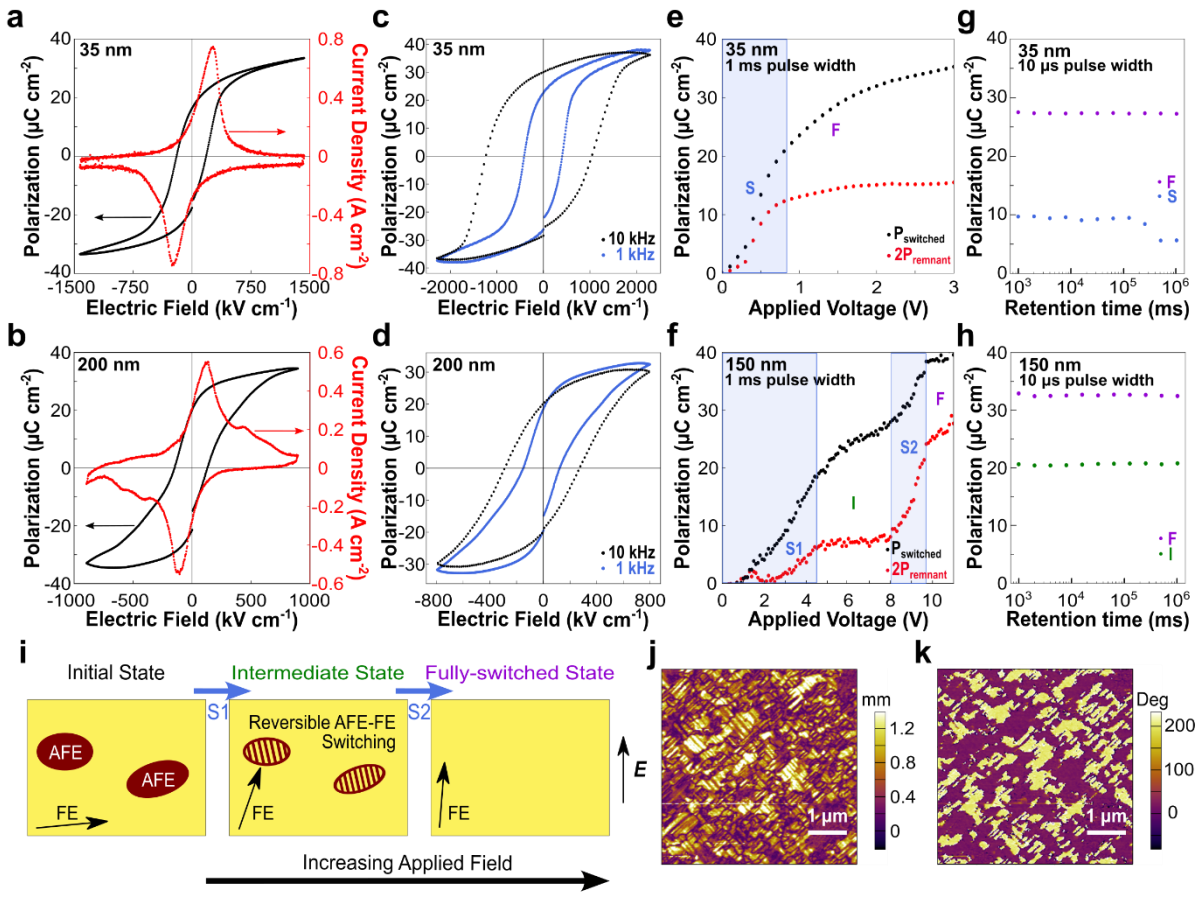

Figure 2. Evidence of a stable intermediate state at intermediate thicknesses. a,b) Ferroelectric hysteresis loop and corresponding switching current curve measured at 1 kHz for (a) 35 nm and (b) 200 nm $NaNbO_3$. c,d) Frequency dependence of ferroelectric hysteresis loops for (c) 35 nm and (d) 200 nm $NaNbO_3$. e,f) Evolution of switched and remnant polarizations from PUND measurements as a function of applied voltage with a 1 ms pulse width for (e) 35 nm and (f) 150 nm $NaNbO_3$. $P_{switched}$ is measured directly from the pulse train in Figure S8, while $2P_{remnant}$ is calculated as $P_{switched} - P_{unswitched}$. g,h) Retention measurements probing the polarization states in different voltage regimes with 10 μs pulse widths for (g) 35 nm [1 V for sub-switching (*S*); 5 V for fully switched (*F*)] and (h) 150 nm $NaNbO_3$ [8 V for intermediate state (*I*); 15 V for fully switched (*F*)]. i) Schematic of possible switching mechanism under increasing applied field in intermediate thickness films with mixed AFE and FE phases. Labels *S1*, Intermediate (*I*), *S2*, and Fully-switched (*F*) correspond to the voltage regimes in (f). j,k) Lateral PFM (j) amplitude and (k) phase images of the 100 nm $NaNbO_3$ film exhibiting a strong in-plane FE response without phase segregation.

To better understand the thickness dependence of the electrical behavior of films, we conducted PUND and retention measurements, with the corresponding pulse sequences in

Figure S8. We carried out PUND measurements with 1 ms pulse width as a function of pulse voltage and measured switched and unswitched polarizations, from which we extract the remnant polarization: $2P_{remnant} = P_{switched} - P_{unswitched}$. PUND measurements on the 35 nm film (Figure 2e) reveal two regimes in the voltage dependence: a sub-switching regime (*S*) at lower voltages, where polarization increases with voltage, and a fully-switched state (*F*) at higher voltages, where the remnant polarization plateaus. The slower, continued increase of switched polarization in the fully-switched state is attributed to leakage currents. Corresponding retention measurements at 1 V and 5 V with a pulse width of 10 μs (Figure 2g) show that the polarization in the sub-switching regime exhibits poorer retention than in the fully-switched state. In contrast, PUND measurements on the intermediate thickness of 150 nm (Figure 2f) exhibit multistate switching with an additional, stable intermediate state, resulting in four distinct regimes in the voltage dependence: two sub-switching regimes (*S1* and *S2*) as well as intermediate (*I*) and fully-switched (*F*) states. Corresponding retention measurements (Figure 2h) taken at 8 V and 15 V show that the polarization of both the intermediate and fully-switched states are equivalently stable.

What causes this stable intermediate state in intermediate thickness films? Based on the presence of the AFE phase in intermediate thickness films from structural characterization, here we propose a potential mechanism for the multistate switching arising from competition between the FE and AFE ferroic orders. Figure 2i illustrates a possible schematic for the film response under increasing out-of-plane electric field. The proposed initial state at zero field has randomly distributed clusters of AFE phase within the FE phase, which has a canted, predominately in-plane polarization, based on both the structural characterization and the PFM measurements (Figure 2j,k and Figure S9) which do not show lateral segregation between AFE and FE phases. In particular, the *Cc* phase is predicted to have a stronger in-plane polarization along $[110]_{pc}$ with a weaker out-of-plane polarization when strained to $SrTiO_3$,[13] matching our experimental results.

Upon initial field application, the FE phase response dominates, leading to increasing switched and remnant polarizations throughout the sub-switching regime *S1* (Figure 2f). At a critical field, dependent on the film thickness but independent of pulse width (Figure S10 and S11), the film transitions to the intermediate state *I* where the applied electric field triggers a reversible AFE-to-FE transition that does not increase the remnant polarization, since removing the applied field causes an immediate relaxation back to the coexistence of AFE and FE phases, leading to the plateau in remnant polarization in Figure 2f. At higher applied fields, the FE-to-AFE transition becomes less stable in sub-switching regime *S2*, leading to

increases in both the switched and remnant polarizations until saturation in the fully-switched state (*F*). This change in the stability of the AFE-FE transition was also observed in the field dependence of *P-E* hysteresis (Figure S12), where a small increase in the maximum applied field leads to a drastic increase in the remnant polarization for the intermediate thicknesses, indicating that the reverse FE-to-AFE transition has been destabilized. However, unlike bulk $NaNbO_3$ ceramics,[30] the AFE-to-FE transition is not irreversible after fields in the *S2* and *F* regime are applied: subsequent measurements with maximum fields in the intermediate regime still show reduced remnant polarization in both *P-E* hysteresis and PUND measurements, indicating the films can be returned to a coexistence of AFE and FE phases. This can be directly observed in Figure S13, where PUND measurements were performed sequentially with the pulse voltage being varied from the intermediate state to the fully-switched state and then back to the intermediate state. The ability to deterministically access either state verifies that reversibility of the AFE-to-FE transition has been maintained even after entering the fully-switched state. Notably, a complete PUND pulse sequence (Figure S8) was performed at each data point using a procedure adapted from a previous work,[32] with the negative preset pulse providing a reversal field which is required to enable the FE-to-AFE transition from the fully-switched state.

Thus, the reversibility of the AFE-to-FE transition is distinct between the intermediate state and the fully-switched state. From the intermediate state, the transition is reversible upon removal of the applied field while from the fully-switched state the transition becomes reversible only upon application of a reversal field, leading to the higher remnant polarization of the fully-switched state. We note that the above discussion is somewhat phenomenological, and further work is needed to fully understand the microscopic mechanism of the intermediate state during switching.

For confirmation of the role of the AFE phase in the underlying switching mechanism, we performed FORC measurements across the thickness range. For each sample, a positive saturating field (E_{sat}) was applied to set the polarization state, with the magnitude determined from PUND measurements. Minor hysteresis loops were recorded by ramping down the electric field to varying reversal fields (E_r) and then increasing it back to E_{sat} while measuring the polarization $p(E,E_r)$ (Experimental Section). Selected sequences of minor hysteresis loops obtained from these measurements are shown in Figure 3a-c. FORC distributions are obtained by taking mixed partial derivatives of $p(E, E_r)$ with respect to E and E_r (Figure 3d-f). In connection to the classical Preisach formalism, this can be interpreted as a density distribution of the macroscopic hysteretic system's elementary switchable units, hysterons, each of which

is characterized by a rectangular hysteresis loop with a coercive field ($E_c = (E - E_r)/2$) and internal bias field ($E_b = (E + E_r)/2$).[45] In Figure 3d-f, the 'reversible' switchable units lie along the E_b axis and the 'irreversible' switchable units have some component along the E_c axis.

For the 35 nm and 250 nm samples, we observe results that align with previous work on classical ferroelectric systems,[45,46] with the minor hysteresis loops (Figure 3a,c) switching from negative to positive polarization across a narrow range of fields. In the FORC distributions (Figure 3d,f), there is a strong peak along the E_c axis arising from irreversible hysterons associated with ferroelectric switching. This is well separated from a secondary peak from reversible hysterons along the E_b axis. Due to the data collection density and numerical methods for calculating the derivatives, some parts of the reversible peaks are cut off. Additionally, some asymmetry along the E_b axis can be observed, either due to the positive poling of the samples or a preferential polarization for the hysterons near the bottom electrode interface.

FORC measurements performed at an intermediate thickness of 150 nm show notable differences, with the minor hysteresis loops (Figure 3b) displaying a variation in the positive switching fields of different minor hysteresis loops. In the FORC distribution, the ferroelectric peak along the coercive field axis is still present, but there exists an additional irreversible peak at (E, E_r) = (225 kV cm^{-1}, -676 kV cm^{-1}) that signifies a clear deviation from the microscopic switching distributions of a traditional ferroelectric. This peak has large components along both the E_c and E_b axes and can be attributed to the reversible AFE-to-FE transition.[47] We note that a similar peak near (E, E_r) = (676 kV cm^{-1}, -225 kV cm^{-1}) is expected but could not be measured due to leakage limitations of the sample that prevented application of positive electric fields above 640 kV cm^{-1} for the 150 nm sample during the FORC measurement procedure . Additionally, the asymmetry along the E_b axis observed in the purely ferroelectric samples may also affect the locations of the antiferroelectric-ferroelectric transition peaks. Regardless, the two peaks in Figure 3e demonstrate that hysterons from both coexisting FE and AFE phases in this intermediate thickness contribute to the film's switching response.

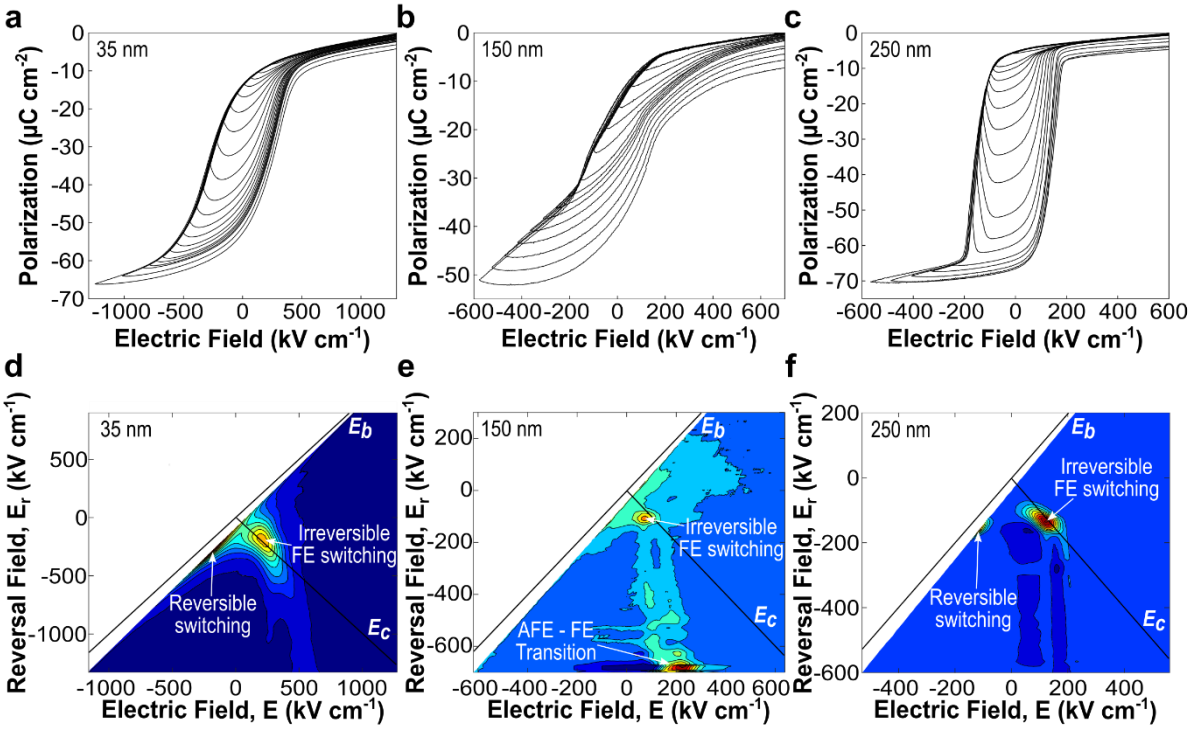

Figure 3. $NaNbO_3$ switching characteristics from FORC measurements. a-c) Selected minor hysteresis loops measured from a positive saturating field to varying reversal fields E_r for (a) 35 nm, (b) 150 nm, and (c) 250 nm $NaNbO_3$ films. d-f) Calculated FORC distributions for (d) 35 nm, (e) 150 nm, and (f) 250 nm $NaNbO_3$ films revealing a peak from ferroelectric switching across all thicknesses with an addition antiferroelectric-ferroelectric transition peak in the intermediate 150 nm film.

2.3. Evaluating application potential across the thickness range

The complex switching mechanism arising from the coexisting AFE and FE phases in the intermediate thicknesses leads to a markedly different voltage dependence of the hysteresis loops compared to a classical ferroelectric. In the 35 nm film, the coercive field and remnant polarization remain approximately constant once the applied field exceeds the coercive field of the fully-switched state (Figure 4a). However, in the 150 nm film, an applied field dependence of the coercive field and remnant polarization persists even once the applied field exceeds the coercive field of the fully-switched state (Figure 4b). This is due to the disruption of the long-range order of the FE phase by the AFE phase when the switching remains within the intermediate state, leading to a lower coercive field and remnant polarization than in the fully-switched state.[48,49]

From these thickness- and voltage-dependent hysteresis loops, we identify two distinct pathways for size effects in strained $NaNbO_3$ films to enhance energy storage properties

relative to the bulk. First, the recoverable energy density is dramatically enhanced by reducing thickness, as seen in Figure 4c, with the 35 nm film outperforming the 250 nm film at 1 kHz by more than five times while offering a modest boost in energy efficiency (Figure 4d). Second, the energy efficiency at intermediate thickness films can be significantly improved by leveraging the pinched and narrow hysteresis loops from the thickness- and strain-stabilized AFE-FE phase coexistence (Figure S12 and S14) through reduction of the maximum applied field. This enables a nearly 3-fold increase in the energy efficiency at 150 nm compared to the fully switched state (Figure 4d) and is accompanied by a small improvement in recoverable energy density (Figure 4c) as well as a significant reduction in coercive field leading to a deviation from Janovec-Kay-Dunn-like behavior[50] (Figure S15).

Altering the frequency enables even further improvements, with the 35 nm film surpassing a recoverable energy density of 20 J cm^{-3} at 10 kHz and the intermediate state in the 150 nm film exhibiting an efficiency of 90% at 100 Hz, each comparable to the highest reported values in pure $NaNbO_3$ and $NaNbO_3$-based ceramics (Figure 4e, Figure S16, and Table S1).[25,30,51–73] Both routes significantly improve both the recoverable energy density and energy efficiency relative to the poor performance of bulk $NaNbO_3$, but not simultaneously in a single film. For practical applications, either reducing thickness or stabilizing an intermediate state from the FE-AFE phase coexistence could be applied to epitaxial thin films of better performing, chemically-substituted $NaNbO_3$-based ceramics to maximize both parameters simultaneously.

In intermediate thickness films with multistate switching, the stable intermediate state is also found to be nearly fatigue-free, despite the films themselves experiencing fatigue when operating at full switching (Figure 4f and Figure S8). This strong fatigue performance, combined with good retention of both the fully-switched and intermediate states in Figure 2h, demonstrates the potential for AFE-FE phase coexistence as a mechanism for generating multiple accessible polarization states for enhanced non-volatile memories.

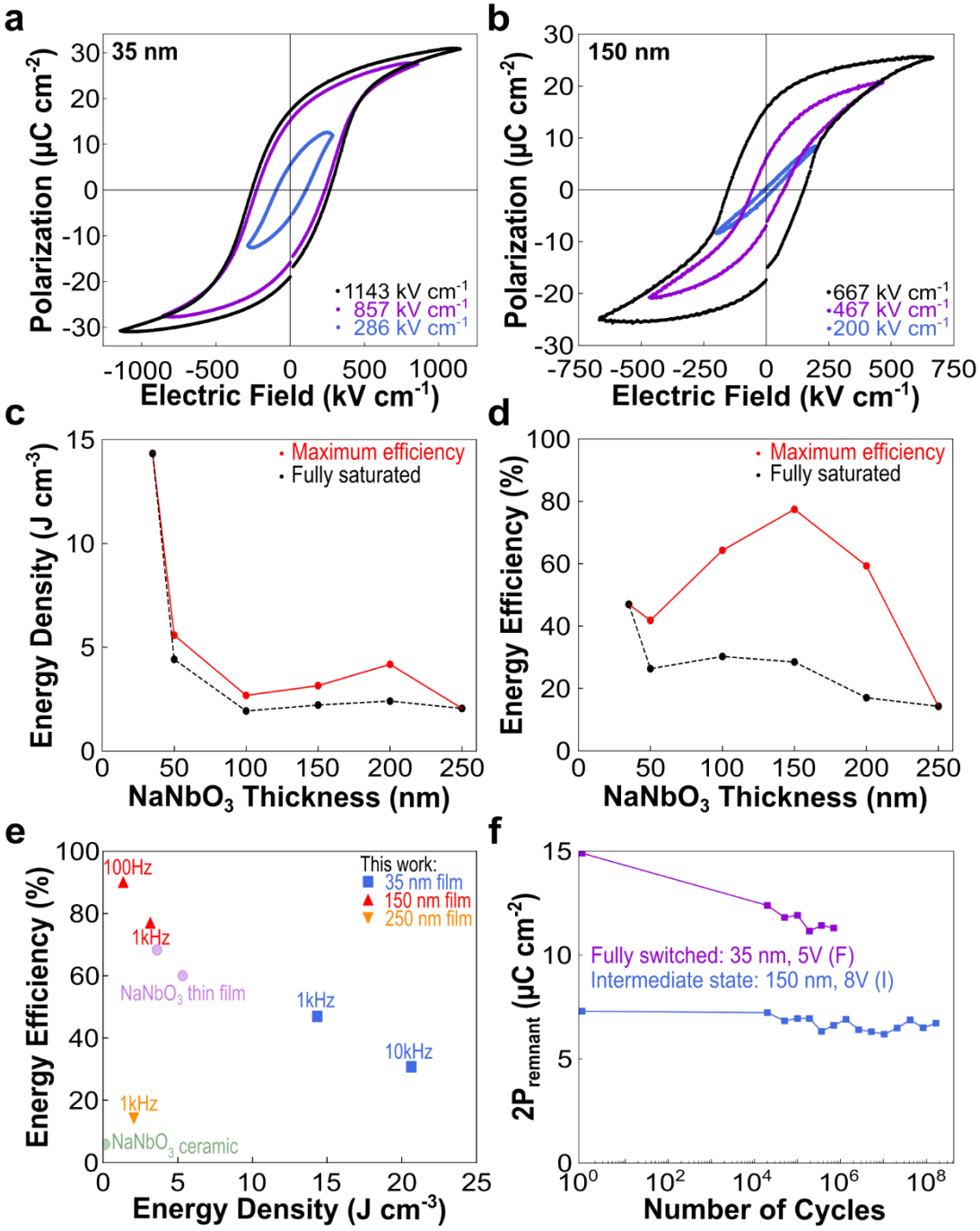

Figure 4. Application potential of $NaNbO_3$ thin films. a,b) Applied field dependence of ferroelectric hysteresis loops for (a) 35 nm $NaNbO_3$ and (b) 150 nm $NaNbO_3$. c,d) Recoverable energy density (c) and energy efficiency (d) as a function of thickness for fully saturated loops (black) and loops achieving maximum efficiency at each thickness through choice of smaller applied field (red), including intermediate switching states (all measured at 1 kHz, corresponding loops and applied electric fields are provided in Figure S12 and S14). e) Comparison of energy storage properties of various $NaNbO_3$ samples including this work as

well as literature reports of ceramic $NaNbO_3$ (green) and other $NaNbO_3$ and $NaNbO_3$-based thin films (purple) (data provided in Table S1). f) Fatigue measurements for a fully switched polarization state of 35 nm $NaNbO_3$ and an intermediate polarization state of 150 nm $NaNbO_3$.

3. Conclusion

In summary, we demonstrate the effects of thickness scaling under coherent epitaxial strain on the ferroic order and electrical properties of $NaNbO_3$ thin films with high crystallinity and low leakage currents. Increasing thickness initially leads to a transition from a single ferroelectric phase to a coexistence of ferroelectric and antiferroelectric phases that displays multistate switching. The intermediate switching state is found to enable multiple accessible remnant polarizations with strong retention and fatigue performance. With a further thickness increase, we find a mixed orientation structure that appears as a strain relief mechanism and suppresses antiferroelectricity, leading to purely ferroelectric behavior in the 250 nm thick film. Evaluating the energy storage properties over the thickness range reveals two pathways by which these strained thin films improve the properties of bulk $NaNbO_3$: improving the energy storage density through miniaturization (crossing 20 J cm^{-3} for 35 nm $NaNbO_3$) and improving the energy efficiency using the complex switching mechanism from the ferroelectric-antiferroelectric phase coexistence (reaching up to 90% at 150 nm). Future work could apply such techniques to further enhance the improvements in chemically substituted antiferroelectric systems that optimize bulk performance.

4. Experimental Section

Thin film synthesis: Tri-layer epitaxial heterostructures of $La_{0.7}Sr_{0.3}MnO_3$ (10 nm thick) / $NaNbO_3$ (35-250 nm thick) / $La_{0.7}Sr_{0.3}MnO_3$ (25 nm thick) were synthesized on (001)-oriented single-crystalline $SrTiO_3$ substrates via pulsed laser deposition in a single chamber with a KrF excimer laser (λ = 248 nm). The polycrystalline non-stoichiometric $Na_{1.2}NbO_3$ target was prepared by grinding and pressing a mixture of Na_2CO_3 and Nb_2O_5, decarbonating at 950°C for 6 hr, then subsequently regrinding, repressing, and sintering at 950°C for 12 hr. The $La_{0.7}Sr_{0.3}MnO_3$ layers were grown with an oxygen pressure of 200-220 mTorr, a laser fluence of 1.52 J cm^{-2}, an imaged laser spot size of 4.93 mm^2, and a repetition rate of 3 Hz, with the bottom 10 nm layer grown at 700 °C and the top 25 nm layer grown at 600 °C. The $NaNbO_3$ layer was grown at 600 °C with an oxygen pressure of 300–330 mTorr, a laser fluence of 1.82 J cm^{-2}, an imaged laser spot size of 6.1 mm^2, and a repetition rate of 2 Hz.

After growth, the chamber was cooled down to room temperature in 1.5 torr O_2 at a cooling rate of 5 °C min^{-1}.

Structural and surface characterization: The θ–2θ X-ray diffraction scans and 2D reciprocal space maps were measured using an Empyrean diffractometer (Malvern Panalytical) with a monochromatic Cu-Kα1 source (1.540598 Å). Piezoresponse force microscopy (PFM) measurements were taken using a Cypher AFM (Asylum Research) in Vector PFM mode using Ir/Pt-coated conductive tips with a force constant of approximately 2.8 N m^{-1} (Nanosensor, PPP-EFM). All PFM measurements were collected with the PFM tip aligned along the [110] direction of the substrate.

Device fabrication: All electrical properties were measured using symmetric circular capacitors, with the voltage applied to the top electrode and the bottom electrode connected to ground. The 100-micron diameter circular top electrodes were defined by photolithographically patterning AZ 1512 photoresist with 1.2 μm thickness using a Durham Magneto Optics ML3 MicroWriter direct write machine and subsequent acid etching of the top $La_{0.7}Sr_{0.3}MnO_3$ layer in a 1:4 H_3PO_4 (14.8 M) to water solution. Contact was made with the bottom $La_{0.7}Sr_{0.3}MnO_3$ electrode using silver paint after scratching the tri-layer structure with a diamond pen.

Leakage measurements: Leakage currents were performed with a 2400 SourceMeter unit (Keithley) by collecting current – applied voltage curves at room temperature in ambient conditions. The applied voltage was increased at 100 mV s^{-1} to the maximum voltage (either 3 V or 8 V), held for 5 s, then swept to an equivalent negative voltage at the same rate, held for 5 s, and returned to 0 V. For leakage current optimization, 10-16 randomly selected capacitors were measured from each sample to determine the optimal synthesis conditions.

Ferroelectric and dielectric property measurements: Ferroelectric properties were measured using a Precision Multiferroic tester (Radiant Technologies) at room temperature in ambient conditions. PUND measurements were performed using the pulse train in Figure S8a. An initial negative preset pulse was applied to set the polarization state, followed by a pulse delay for the polarization to return to its negative remnant value. This was then followed by a positive switching pulse to measure the full switched polarization (P^*), an additional delay to return to the positive remnant polarization, and a second positive pulse to measure the unswitched polarization ($P^\wedge$). By subtracting the unswitched polarization from the switched polarization, we obtain information regarding the remnant polarization of the film: $2P_{remnant} = P^* - P^\wedge$. For all voltage-dependent PUND measurements, the applied voltage was increased in 100 mV increments with a 1 ms pulse delay and constant pulse width of 1 ms. The pulse

width was kept constant at 1 ms for Fig 2e,f and Figure S10, and was varied between 10 µs, 100 µs, and 1 ms in Figure S11. Retention measurements were taken using the pulse train in Figure S8b at a 10 µs pulse width. Dielectric measurements were taken using an E4980A LCR meter (Agilent Technologies) on poled capacitor structures with 8.6 kV cm^{-1} AC field and 0 V DC bias.

In fatigue measurements, PUND measurements were taken before and after the sample was repeatedly cycled by a switching waveform, as depicted in Figure S8c. The switching waveform was a square wave applied at 10 kHz and the PUND measurements were taken with a 1 ms pulse delay and 100 µs pulse width. The maximum voltage applied for both the switching waveform and the PUND measurement was 5V for the 35 nm $NaNbO_3$ film and 8V for the 150 nm $NaNbO_3$ film.

FORC measurements were recorded using a positive saturating field whose magnitude depended on the sample thickness. The field was lowered to varying reversal fields and then returned to the saturating field at a frequency of 1 kHz while recording the polarization. The polarization $p(E, E_r)$ during the ascending return sweep was used to calculate the FORC distribution $\rho(E, E_r)$ by taking mixed second derivatives with respect to both E and E_r:

$$\rho(E, E_r) = \frac{1}{2}\frac{\partial^2 p(E, E_r)}{\partial E \partial E_r} \quad (1)$$

Energy storage parameters were extracted from the polarization – electric field hysteresis curves by numerically integrating the positive electric field data. Recoverable energy density is given by:

$$W_{rec} = \int_{P_{rem}}^{P_{sat}} E_{descend} dP \quad (2)$$

integrating along the descending branch of the hysteresis curve, while W_{loss} is the area inside the hysteresis curve given by:

$$W_{loss} = \int_{P_{rem}}^{P_{sat}} E_{ascend} dP - W_{rec} \quad (3)$$

From this, we calculate energy storage efficiency:

$$\eta = \frac{W_{rec}}{W_{rec} + W_{loss}} \times 100\% \quad (4)$$

Acknowledgements

A.K. and K.J.C. contributed equally to this work. Work at SLAC/Stanford was supported by the U.S. DOE, Office of Basic Energy Sciences, Division of Materials Sciences and

Engineering, under Contract No. DE-AC02-76SF00515. Part of this work was performed at the Stanford Nano Shared Facilities (SNSF) RRID:SCR_023230, supported by the National Science Foundation under award ECCS-2026822. R.G. and R.X. acknowledge the support from the National Science Foundation (NSF) under award No. DMR-2442399 and the American Chemical Society Petroleum Research Fund under award No. 68244-DNI10.

Conflict of Interest

The authors declare no conflict of interest.

Data Availability Statement

The data that supports the findings of this study are available from the corresponding author upon reasonable request.

Received:

Revised:

Published online:

References

[1] C. A. Randall, Z. Fan, I. Reaney, L. Chen, S. Trolier-McKinstry, "Antiferroelectrics: History, Fundamentals, Crystal Chemistry, Crystal Structures, Size Effects, and Applications," *Journal of the American Ceramic Society* **2021**, *104*, 3775.

[2] Z. Liu, T. Lu, J. Ye, et al., "Antiferroelectrics for Energy Storage Applications: A Review," *Advanced Materials Technologies* **2018**, *3*, 1.

[3] Y. Si, T. Zhang, C. Liu, et al., "Antiferroelectric Oxide Thin-Films: Fundamentals, Properties, and Applications," *Progress in Materials Science* **2024**, *142*, 101231.

[4] C. Kittel, "Theory of Antiferroelectric Crystals," *Physical Review* **1951**, *82*, 729.

[5] M. Tsai, Y. Zheng, S. Lu, et al., "Antiferroelectric Anisotropy of Epitaxial $PbHfO_3$ Films for Flexible Energy Storage," *Advanced Functional Materials* **2021**, *31*, DOI 10.1002/adfm.202105060.

[6] Y. Si, T. Zhang, Z. Chen, et al., "Phase Competition in High-Quality Epitaxial Antiferroelectric PbZrO3Thin Films," *ACS Applied Materials and Interfaces* **2022**, *14*, 51096.

[7] R. Gao, S. E. Reyes-Lillo, R. Xu, et al., "Ferroelectricity in Pb1+δZrO3 Thin Films," *Chemistry of Materials* **2017**, *29*, 6544.

[8] K. E. Johnston, C. C. Tang, J. E. Parker, K. S. Knight, P. Lightfoot, S. E. Ashbrook, "The Polar Phase of NaNbO3: A Combined Study by Powder Diffraction, Solid-State NMR, and First-Principles Calculations," *Journal of the American Chemical Society* **2010**, *132*, 8732.

[9] S. K. Mishra, N. Choudhury, S. L. Chaplot, P. S. R. Krishna, R. Mittal, "Competing Antiferroelectric and Ferroelectric Interactions in NaNbO3: Neutron Diffraction and Theoretical Studies," *Physical Review B* **2007**, *76*, 024110.

[10] M.-H. Zhang, L. Fulanović, C. Zhao, J. Koruza, "Review on Field-Induced Phase Transitions in Lead-Free NaNbO3-Based Antiferroelectric Perovskite Oxides for Energy Storage," *Journal of Materiomics* **2023**, *9*, 1.
[11] R. H. Dungan, R. D. Golding, "Metastable Ferroelectric Sodium Niobate," *Journal of the American Ceramic Society* **1964**, *47*, 73.
[12] T. Schneider, J. Cardoletti, P. Komissinskiy, L. Alff, " Impact of Strain Engineering on Antiferroelectricity in NaNbO 3 Thin Films ," *ACS Omega* **2023**, DOI 10.1021/acsomega.3c01327.
[13] K. Patel, S. Prosandeev, B. Xu, C. Xu, L. Bellaiche, "Properties of (001) NaNbO3 Films under Epitaxial Strain: A First-Principles Study," *Physical Review B* **2021**, *103*, 094103.
[14] O. Diéguez, K. M. Rabe, D. Vanderbilt, "First-Principles Study of Epitaxial Strain in Perovskites," *Physical Review B - Condensed Matter and Materials Physics* **2005**, *72*, DOI 10.1103/PhysRevB.72.144101.
[15] H. D. Megaw, "The Seven Phases of Sodium Niobate," *Ferroelectrics* **1974**, *7*, 87.
[16] H. KP, R. Xu, K. Patel, et al., "Electron Ptychography Reveals a Ferroelectricity Dominated by Anion Displacements," *Nature Materials* **2025**, DOI 10.1038/s41563-025-02205-x.
[17] Y. I. Yuzyuk, R. A. Shakhovoy, S. I. Raevskaya, et al., "Ferroelectric Q-Phase in a NaNbO3 Epitaxial Thin Film," *Applied Physics Letters* **2010**, *96*, 96.
[18] J. Sellmann, J. Schwarzkopf, A. Kwasniewski, M. Schmidbauer, D. Braun, A. Duk, "Strained Ferroelectric NaNbO3 Thin Films: Impact of Pulsed Laser Deposition Growth Conditions on Structural Properties," *Thin Solid Films* **2014**, *570*, 107.
[19] T. Schneider, J. Cardoletti, H. Ding, et al., "Evidence for Antipolar Displacements in NaNbO3thin Films," *Applied Physics Letters* **2022**, *121*, 0.
[20] Y. I. Yuzyuk, P. Simon, E. Gagarina, et al., "Modulated Phases in NaNbO3: Raman Scattering, Synchrotron x-Ray Diffraction, and Dielectric Investigations," *Journal of Physics Condensed Matter* **2005**, *17*, 4977.
[21] S. Yamazoe, H. Sakurai, M. Fukada, H. Adachi, T. Wada, "The Effect of SrTiO3 Substrate Orientation on the Surface Morphology and Ferroelectric Properties of Pulsed Laser Deposited NaNbO 3 Films," *Applied Physics Letters* **2009**, *95*, DOI 10.1063/1.3205103.
[22] R. Xu, K. J. Crust, V. Harbola, et al., "Size-Induced Ferroelectricity in Antiferroelectric Oxide Membranes," *Advanced Materials* **2023**, *2210562*, 2210562.
[23] J. Schwarzkopf, D. Braun, M. Hanke, R. Uecker, M. Schmidbauer, "Strain Engineering of Ferroelectric Domains in in KxNa1-XNbO3 Epitaxial Layers," *Frontiers in Materials* **2017**, *4*, DOI 10.3389/fmats.2017.00026.
[24] B. Lin, K. P. Ong, T. Yang, et al., "Ultrahigh Electromechanical Response from Competing Ferroic Orders," *Nature* **2024**, DOI 10.1038/s41586-024-07917-9.
[25] H. Dong, B. Luo, K. Jin, "Tunable Dielectric and Energy Storage Properties in Nonstoichiometric NaNbO3 Thin Films," *Ceramics International* **2022**, *48*, 16215.
[26] L. Yang, X. Kong, F. Li, et al., "Perovskite Lead-Free Dielectrics for Energy Storage Applications," *Progress in Materials Science* **2019**, *102*, 72.
[27] J. Ye, G. Wang, X. Chen, F. Cao, X. Dong, "Enhanced Antiferroelectricity and Double Hysteresis Loop Observed in Lead-Free (1−x)NaNbO3-XCaSnO3 Ceramics," *Applied Physics Letters* **2019**, *114*, DOI 10.1063/1.5080538.
[28] J. Ma, J. Zhang, J. Guo, et al., "Achieving Ultrahigh Energy Storage Density in Lead-Free Sodium Niobate-Based Ceramics by Modulating the Antiferroelectric Phase," *Chemistry of Materials* **2022**, *34*, 7313.
[29] N. Luo, L. Ma, G. Luo, et al., "Well-Defined Double Hysteresis Loop in NaNbO3 Antiferroelectrics," *Nature Communications* **2023**, *14*, 1776.

[30] M.-H. Zhang, H. Ding, S. Egert, et al., "Tailoring High-Energy Storage NaNbO3-Based Materials from Antiferroelectric to Relaxor States," *Nature Communications* **2023**, *14*, 1525.
[31] C. Chen, D. Chen, P. Li, et al., "Deterministic Manipulation of Multi-State Polarization Switching in Multiferroic Thin Films," *Advanced Functional Materials* **2023**, *33*, DOI 10.1002/adfm.202208244.
[32] R. Xu, S. Liu, S. Saremi, et al., "Kinetic Control of Tunable Multi-State Switching in Ferroelectric Thin Films," *Nature Communications* **2019**, *10*, DOI 10.1038/s41467-019-09207-9.
[33] D. Lee, B. C. Jeon, S. H. Baek, et al., "Active Control of Ferroelectric Switching Using Defect-Dipole Engineering," *Advanced Materials* **2012**, *24*, 6490.
[34] L. Baudry, I. Lukyanchuk, V. M. Vinokur, "Ferroelectric Symmetry-Protected Multibit Memory Cell," *Scientific Reports* **2017**, *7*, DOI 10.1038/srep42196.
[35] A. R. Damodaran, S. Pandya, J. C. Agar, et al., "Three-State Ferroelastic Switching and Large Electromechanical Responses in PbTiO3 Thin Films," *Advanced Materials* **2017**, *29*, DOI 10.1002/adma.201702069.
[36] J. H. Lee, K. Chu, K. E. Kim, J. Seidel, C. H. Yang, "Out-of-Plane Three-Stable-State Ferroelectric Switching: Finding the Missing Middle States," *Physical Review B* **2016**, *93*, DOI 10.1103/PhysRevB.93.115142.
[37] M. Abazari, A. Safari, "Leakage Current Behavior in Lead-Free Ferroelectric (K,Na)NbO3-LiTaO3-LiSbO3 Thin Films," *Applied Physics Letters* **2010**, *97*, DOI 10.1063/1.3531575.
[38] A. Vailionis, H. Boschker, W. Siemons, et al., "Misfit Strain Accommodation in Epitaxial ABO3 Perovskites: Lattice Rotations and Lattice Modulations," *Physical Review B - Condensed Matter and Materials Physics* **2011**, *83*, DOI 10.1103/PhysRevB.83.064101.
[39] R. Ghanbari, H. KP, K. Patel, et al., "Strain-Induced Lead-Free Morphotropic Phase Boundary," *Nature Communications* **2025**, *16*, 7766.
[40] Q. Fan, C. Ma, C. Ma, R. Lu, S. Cheng, M. Liu, "Manipulating Leakage Behavior via Thickness in Epitaxial BaZr0.35Ti0.65O3thin Film Capacitors," *Applied Physics Letters* **2020**, *116*, DOI 10.1063/1.5145119.
[41] L. Liu, Y. Wang, Z. Hou, R. Lv, "Pinched P–E Hysteresis Loops of KSr2Nb5O15 Ferroelectric Ceramics," *Materials Science and Engineering: B* **2021**, *269*, DOI 10.1016/j.mseb.2021.115174.
[42] K. Kobayashi, M. Ryu, Y. Doshida, Y. Mizuno, C. A. Randall, "Novel High-Temperature Antiferroelectric-Based Dielectric NaNbO3 – NaTaO3 Solid Solutions Processed in Low Oxygen Partial Pressures," *Journal of the American Ceramic Society* **2013**, *96*, 531.
[43] T. Saito, H. Adachi, T. Wada, H. Adachi, "Pulsed-Laser Deposition of Ferroelectric NaNbO3 Thin Films," *Japanese Journal of Applied Physics, Part 1: Regular Papers and Short Notes and Review Papers* **2005**, *44*, 6969.
[44] T. Oikawa, M. Aratani, H. Funakubo, K. Saito, M. Mizuhira, "Composition and Orientation Dependence of Electrical Properties of Epitaxial Pb(ZrxTi1-x)O3 Thin Films Grown Using Metalorganic Chemical Vapor Deposition," *Journal of Applied Physics* **2004**, *95*, 3111.
[45] L. Mitoseriu, L. Stoleriu, A. Stancu, C. Galassi, V. Buscaglia, "First Order Reversal Curves Diagrams for Describing Ferroelectric Switching Characteristics," *Processing and Application of Ceramics* **2009**, *3*, 3.
[46] A. Stancu, D. Ricinschi, L. Mitoseriu, P. Postolache, M. Okuyama, "First-Order Reversal Curves Diagrams for the Characterization of Ferroelectric Switching," *Applied Physics Letters* **2003**, *83*, 3767.

[47] K. Nadaud, C. Borderon, R. Renoud, M. Bah, S. Ginestar, H. W. Gundel, "Study of the Long Time Relaxation of the Weak Ferroelectricity in PbZrO3 Antiferroelectric Thin Film Using Positive Up Negative Down and First Order Reversal Curves Measurements," *Thin Solid Films* **2023**, *773*, DOI 10.1016/j.tsf.2023.139817.
[48] W. Shi, L. Zhang, R. Jing, et al., "Relaxor Antiferroelectric-like Characteristic Boosting Enhanced Energy Storage Performance in Eco-Friendly (Bi0.5Na0.5)TiO3-Based Ceramics," *Journal of the European Ceramic Society* **2022**, *42*, 4528.
[49] M. N. Al-Aaraji, W. N. Hasan, K. Al-Marzoki, "Progress In Lead Free- Relaxor Ferroelectrics For Energy Storage Applications.," *Journal of Physics: Conference Series* **2021**, *1973*, 012117.
[50] P. Chandra, M. Dawber, P. B. Littlewood, J. F. Scott, "Scaling of the Coercive Field with Thickness in Thin-Film Ferroelectrics," *Ferroelectrics* **2004**, *313*, 7.
[51] H. Qi, R. Zuo, A. Xie, et al., "Ultrahigh Energy-Storage Density in NaNbO3-Based Lead-Free Relaxor Antiferroelectric Ceramics with Nanoscale Domains," *Advanced Functional Materials* **2019**, *29*, 11.
[52] Z. Chen, S. Mao, L. Ma, et al., "Phase Engineering in NaNbO3 Antiferroelectrics for High Energy Storage Density," *Journal of Materiomics* **2022**, *8*, 753.
[53] Z. Liu, J. Lu, Y. Mao, P. Ren, H. Fan, "Energy Storage Properties of NaNbO3-CaZrO3 Ceramics with Coexistence of Ferroelectric and Antiferroelectric Phases," *Journal of the European Ceramic Society* **2018**, *38*, 4939.
[54] A. Xie, J. Fu, R. Zuo, et al., "NaNbO3-CaTiO3 Lead-Free Relaxor Antiferroelectric Ceramics Featuring Giant Energy Density, High Energy Efficiency and Power Density," *Chemical Engineering Journal* **2022**, *429*, 132534.
[55] H. Qi, A. Xie, A. Tian, R. Zuo, "Superior Energy-Storage Capacitors with Simultaneously Giant Energy Density and Efficiency Using Nanodomain Engineered $BiFeO_3$ -$BaTiO_3$ -$NaNbO_3$ Lead-Free Bulk Ferroelectrics," *Advanced Energy Materials* **2020**, *10*, DOI 10.1002/aenm.201903338.
[56] J. Lei, Y. Zhang, Z. Li, et al., "Giant Energy Density with Ultrahigh Efficiency Achieved in NaNbO3-Based Lead-Free Ceramics with Polymorphic Antiferrodistortive Polar Nanodomains," *Chemical Engineering Journal* **2024**, *498*, 155803.
[57] S. Zhang, W. Li, Y. Zhang, X. Tang, Y. Jiang, X. Guo, "Excellent Energy Density and Power Density Achieved in NaNbO3-Based Relaxor Ferroelectric Ceramics," *Materials Science and Engineering: B* **2024**, *299*, 117025.
[58] C. Sun, X. Chen, J. Shi, et al., "Simultaneously with Large Energy Density and High Efficiency Achieved in NaNbO3-Based Relaxor Ferroelectric Ceramics," *Journal of the European Ceramic Society* **2021**, *41*, 1891.
[59] H. Qi, R. Zuo, A. Xie, J. Fu, D. Zhang, "Excellent Energy-Storage Properties of NaNbO3-Based Lead-Free Antiferroelectric Orthorhombic P-Phase (Pbma) Ceramics with Repeatable Double Polarization-Field Loops," *Journal of the European Ceramic Society* **2019**, *39*, 3703.
[60] J. Jiang, X. Meng, L. Li, et al., "Enhanced Energy Storage Properties of Lead-Free NaNbO3-Based Ceramics via A/B-Site Substitution," *Chemical Engineering Journal* **2021**, *422*, 130130.
[61] S. Zhang, W. Li, Y. Zhang, X. Tang, Y. Jiang, X. Guo, "Large Energy Density and High Efficiency Achieved Simultaneously in Bi(Mg0.5Hf0.5)O3-Modified NaNbO3 Ceramics," *Results in Physics* **2023**, *44*, 106194.
[62] A. Xie, J. Lei, Y. Zhang, et al., "Collaboratively Improved Energy Density and Efficiency in NaNbO3-Based Lead-Free Relaxor Ferroelectrics via Enhancing Antiferrodistortion," *Journal of Materials Chemistry A* **2024**, *12*, 9124.
[63] A. Xie, R. Zuo, Z. Qiao, Z. Fu, T. Hu, L. Fei, "$NaNbO_3$ -$(Bi_{0.5}Li_{0.5})TiO_3$ Lead-Free Relaxor Ferroelectric Capacitors with Superior Energy-Storage Performances via

Multiple Synergistic Design," *Advanced Energy Materials* **2021**, *11*, DOI 10.1002/aenm.202101378.
[64] J. Ye, G. Wang, M. Zhou, et al., "Excellent Comprehensive Energy Storage Properties of Novel Lead-Free NaNbO3-Based Ceramics for Dielectric Capacitor Applications," *Journal of Materials Chemistry C* **2019**, *7*, 5639.
[65] W. Yang, H. Zeng, F. Yan, et al., "Microstructure-Driven Excellent Energy Storage NaNbO3-Based Lead-Free Ceramics," *Ceramics International* **2022**, *48*, 37476.
[66] J. Wang, X. Nie, Z. Peng, et al., "Ultra-Fast Charge-Discharge and High Energy Storage Density Realized in NaNbO3–La(Mn0.5Ni0.5)O3 Ceramics," *Ceramics International* **2021**, *47*, 28493.
[67] J. Shi, X. Chen, X. Li, et al., "Realizing Ultrahigh Recoverable Energy Density and Superior Charge-Discharge Performance in NaNbO3-Based Lead-Free Ceramics: Via a Local Random Field Strategy," *Journal of Materials Chemistry C* **2020**, *8*, 3784.
[68] M. Zhou, R. Liang, Z. Zhou, S. Yan, X. Dong, "Novel Sodium Niobate-Based Lead-Free Ceramics as New Environment-Friendly Energy Storage Materials with High Energy Density, High Power Density, and Excellent Stability," *ACS Sustainable Chemistry and Engineering* **2018**, *6*, 12755.
[69] J. Ma, D. Zhang, F. Ying, et al., "Ultrahigh Energy Storage Density and High Efficiency in Lead-Free (Bi0.9Na0.1)(Fe0.8Ti0.2)O3-Modified NaNbO3Ceramics via Stabilizing the Antiferroelectric Phase and Enhancing Relaxor Behavior," *ACS Applied Materials and Interfaces* **2022**, *14*, 19704.
[70] R. Zhao, K. Wang, W. Li, et al., "High Recoverable Energy Storage Density and Efficiency Achieved in Doped NaNbO3 Ceramics via Composition Design Strategy for Pulsed Power Capacitor," *Chemical Engineering Journal* **2024**, *495*, 153421.
[71] L.-F. Zhu, Y. Yan, H. Leng, X. Li, L.-Q. Cheng, S. Priya, "Energy-Storage Performance of $NaNbO_3$ Based Multilayered Capacitors," *Journal of Materials Chemistry C* **2021**, *9*, 7950.
[72] P. Zhao, L. Li, X. Wang, "BaTiO3-NaNbO3 Energy Storage Ceramics with an Ultrafast Charge-Discharge Rate and Temperature-Stable Power Density," *Microstructures* **2022**, *3*, 2022023.
[73] Y. Zhang, Y. Niu, Y. Sun, Z. Sun, Z. Yu, "Effect of Annealing Temperature on Energy Storage Performance of NaNbO3-Based Thin Films under Pure Oxygen," *Applied Physics A* **2024**, *130*, 676.

Supporting Information

Supporting Information is available from the Wiley Online Library or from the author.

Supporting Information

Coexisting Phases in $NaNbO_3$ Thin Films Influenced by Epitaxial Strain and Size Effects

Aarushi Khandelwal, Kevin J. Crust, Reza Ghanbari, Yijun Yu, Ruijuan Xu*, and Harold Y. Hwang*

Figure S1

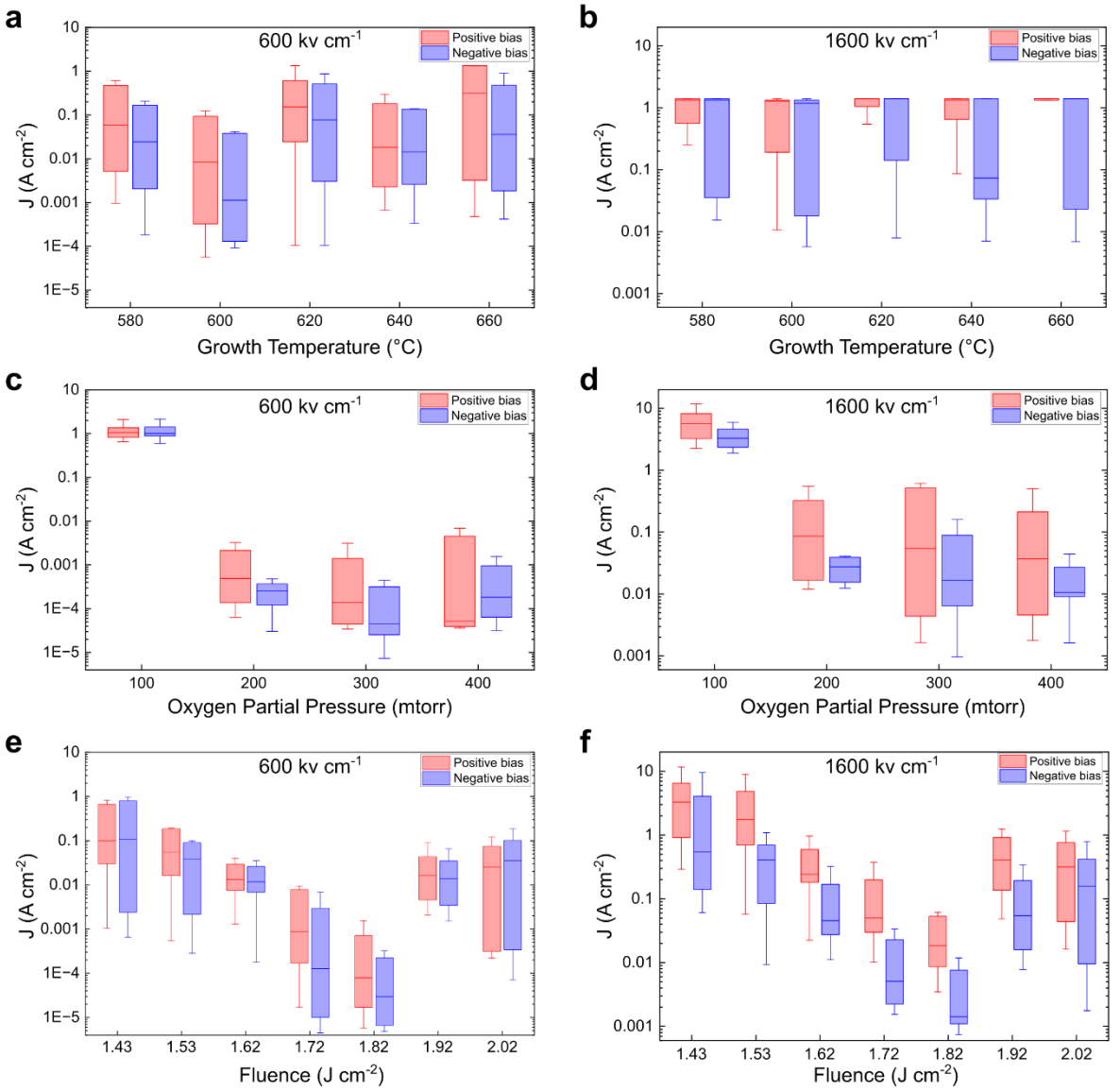

Figure S1. Leakage current optimization. Box charts displaying the distributions of current densities measured from randomly selected capacitors in $La_{0.7}Sr_{0.3}MnO_3$ / $NaNbO_3$ / $La_{0.7}Sr_{0.3}MnO_3$ / $SrTiO_3$ heterostructures. The (a,b) temperature, (c,d) oxygen partial pressure, and (e,f) fluence of the 50 nm $NaNbO_3$ layer were varied to determine the optimal synthesis conditions. Leakage currents were extracted from current – voltage (IV) measurements at maximum electric fields of (a,c,e) 600 kV cm^{-1} and (b,d,f) 1600 kV cm^{-1}. The box plots the lower quartile, median, and upper quartile, while the upper (lower) whisker plots the outermost data point within the 75^{th} percentile + 1.5 * interquartile range (25^{th} percentile – 1.5 * interquartile range).

Figure S2

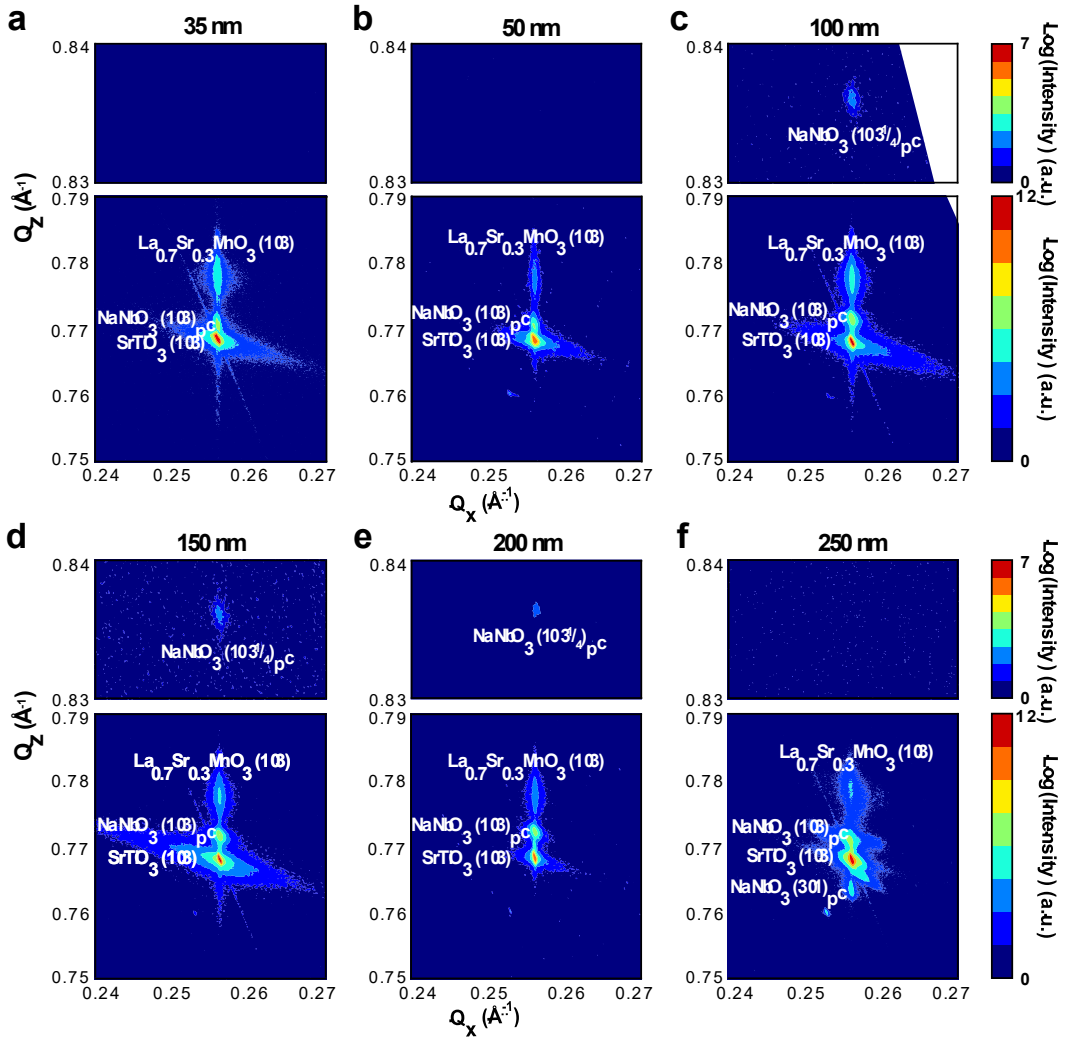

Figure S2. Thickness dependence of film orientation and phase from structural characterization. X-ray reciprocal space maps about the $SrTiO_3$ (103) diffraction condition for heterostructures with (a) 35, (b) 50, (c) 100, (d) 150, (e) 200, and (f) 250 nm thick $NaNbO_3$.

Figure S3

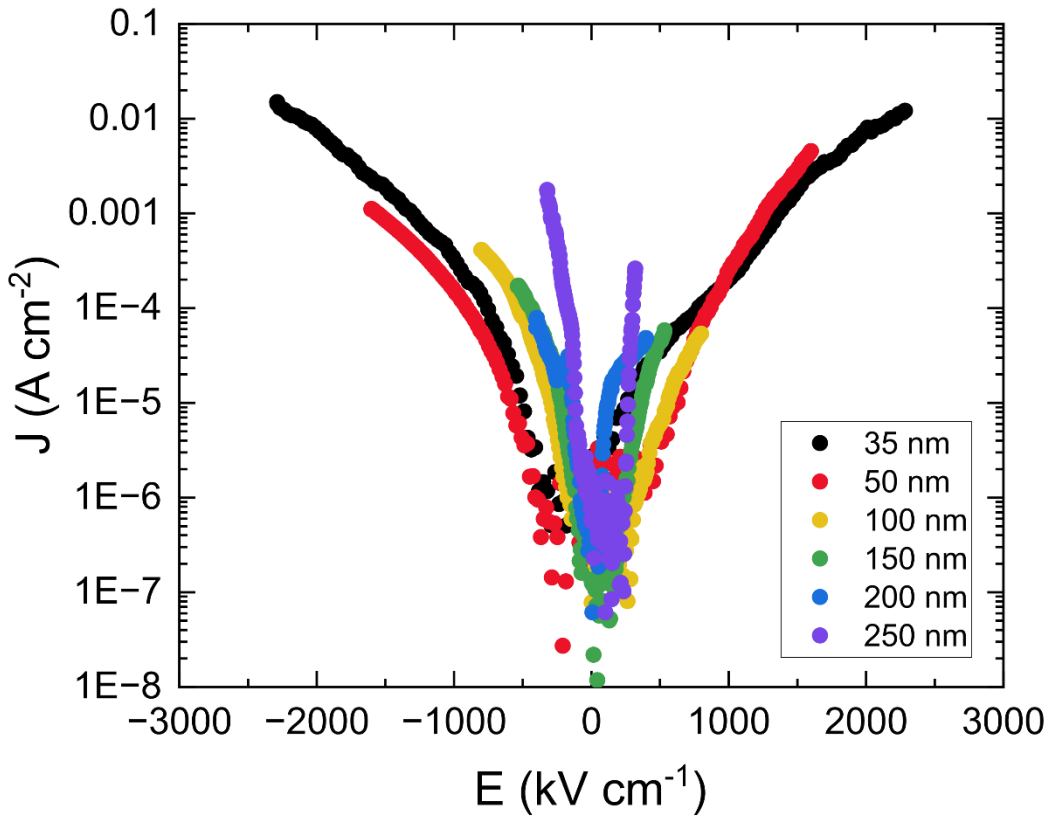

Figure S3. Thickness dependence of leakage current. Current – voltage measurements, converted into current density – electric field, of the $La_{0.7}Sr_{0.3}MnO_3$ / $NaNbO_3$ / $La_{0.7}Sr_{0.3}MnO_3$ capacitors with varying $NaNbO_3$ film thickness. A maximum of 8 V was applied to each capacitor, leading to a reduction in the maximum applied field with increasing thickness.

Figure S4

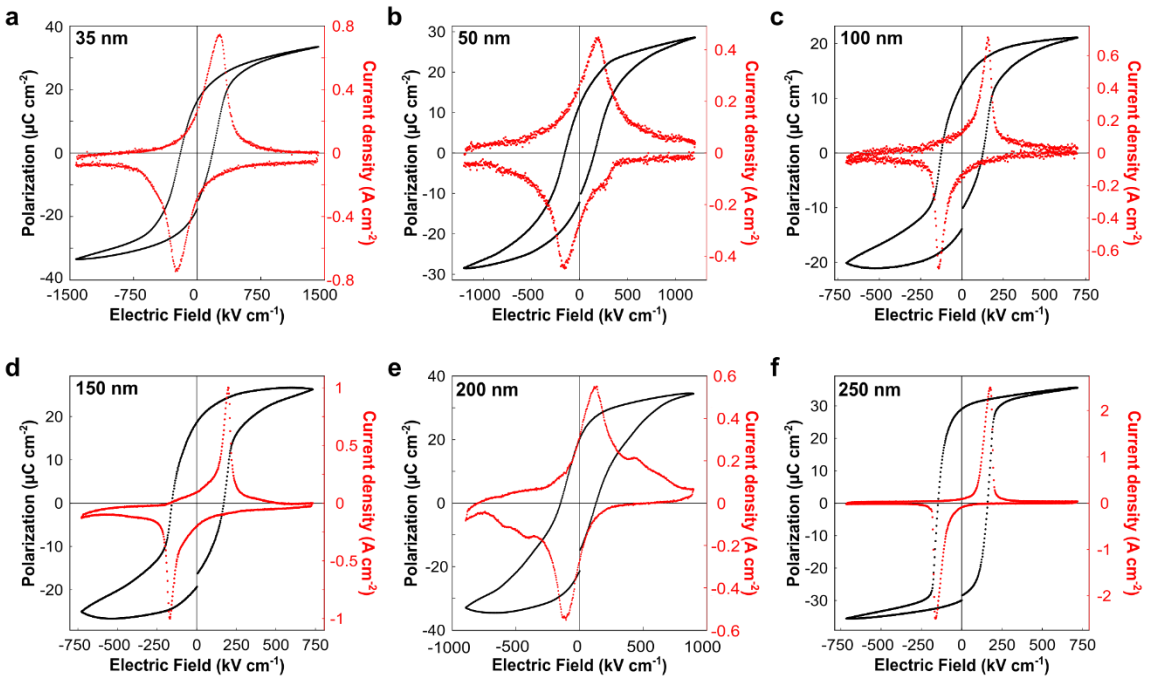

Figure S4. Thickness dependence of ferroelectric hysteresis loops. Polarization – electric field hysteresis measurements and corresponding switching current – electric field hysteresis measurements at 1 kHz for (a) 35, (b) 50, (c) 100, (d) 150, (e) 200, and (f) 250 nm thick $NaNbO_3$.

Figure S5

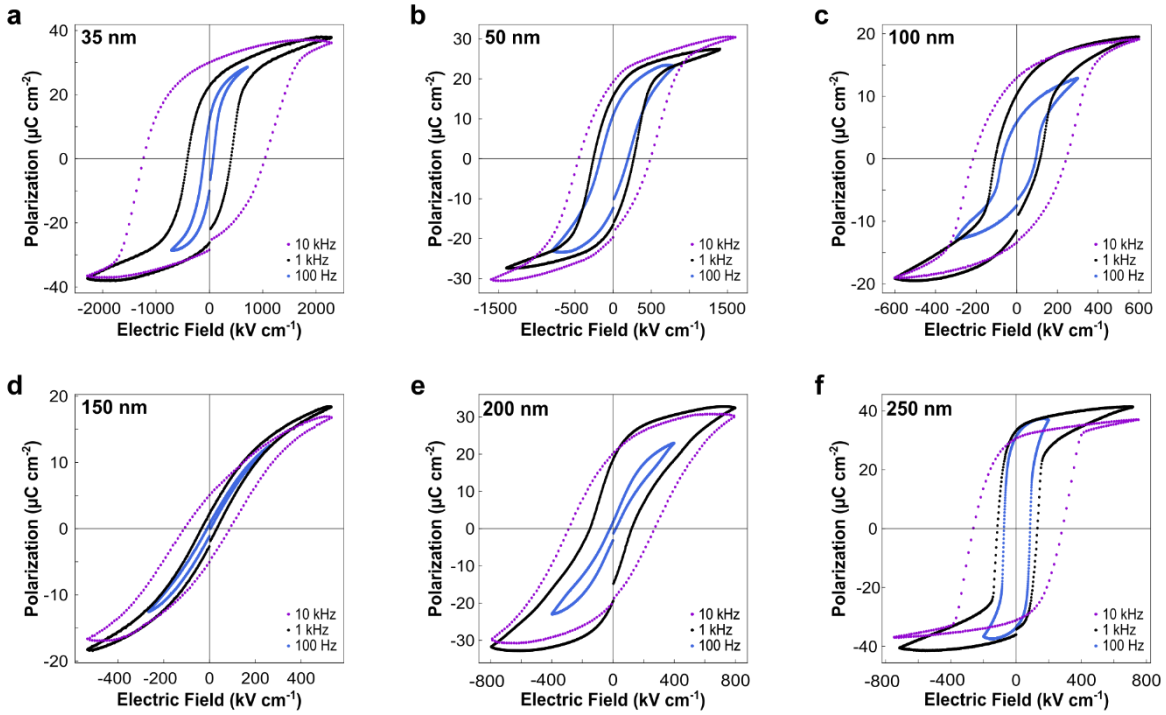

Figure S5. Frequency dependence of ferroelectric hysteresis. Polarization – electric field hysteresis loops for (a) 35, (b) 50, (c) 100, (d) 150, (e) 200, and (f) 250 nm thick $NaNbO_3$.

Figure S6

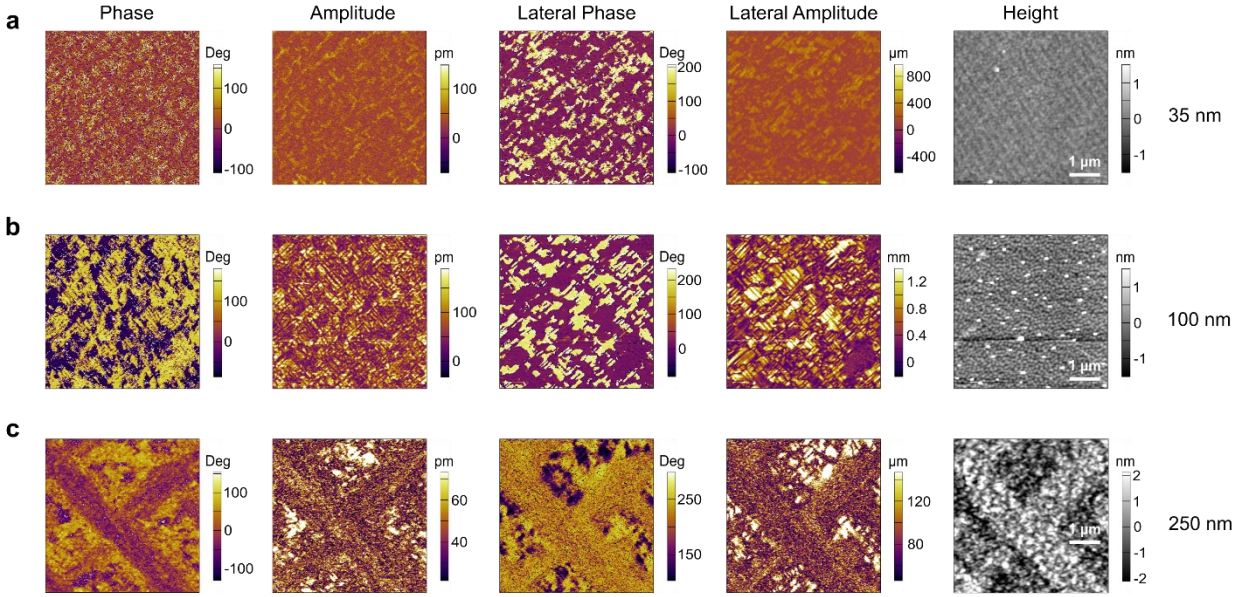

Figure S6. Thickness dependence of piezoresponse force microscopy. Vertical phase, vertical amplitude, lateral phase, lateral amplitude, and topography piezoresponse force microscopy (PFM) images of $NaNbO_3$ / $La_{0.7}Sr_{0.3}MnO_3$ / $SrTiO_3$ heterostructures with various thicknesses of $NaNbO_3$. The (a) 35 nm and (b) 100 nm samples show atomically smooth surfaces with clear domain patterns and stronger in-plane polarization. The (c) 250 nm sample shows laterally segregated regions with different heights, which is attributed to the separate peaks observed in the X-ray structural characterization. The lower region continues to show stronger in-plane polarization with clear domains, while the higher region shows a relatively stronger out-of-plane polarization signal. Images are collected with the PFM tip aligned along the [110] direction of the substrate.

Figure S7

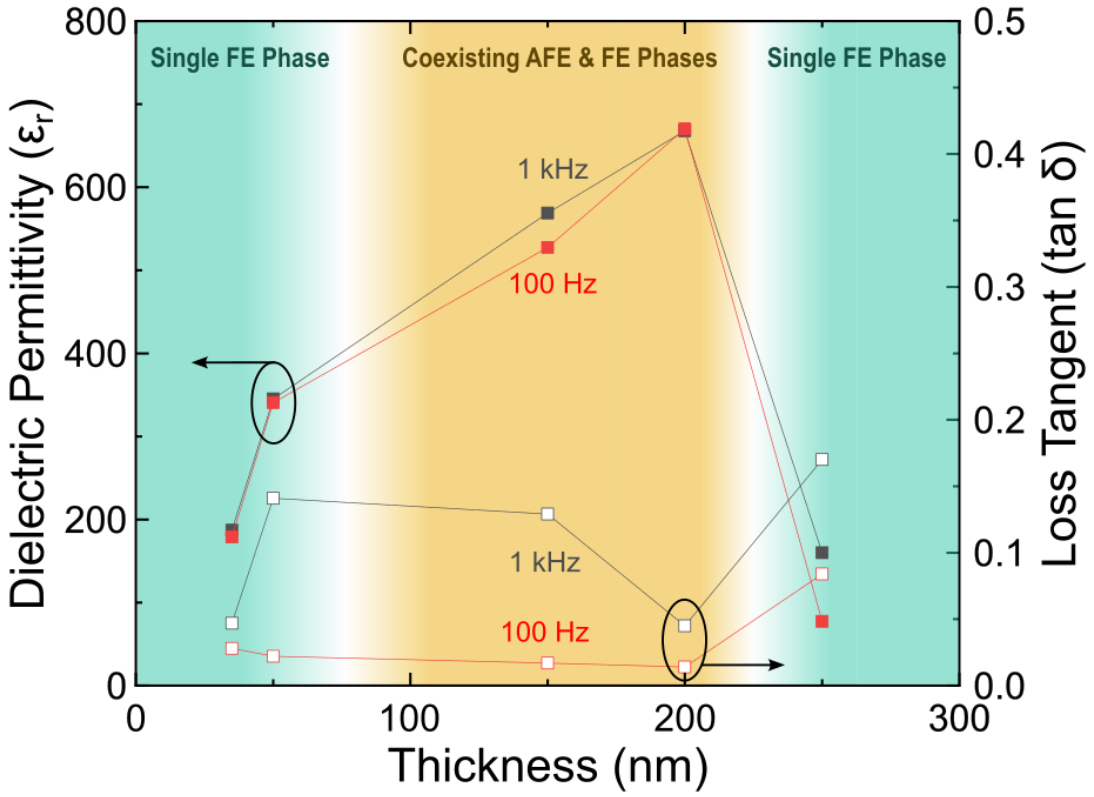

Figure S7. Thickness dependence of dielectric permittivity and loss tangent at 1 kHz and 100 Hz. Relative dielectric permittivity and loss tangent of poled $NaNbO_3$ at various thicknesses, measured at 0 V DC bias. The permittivity is significantly increased in the thicknesses where an antiferroelectric quarter-order superlattice reflection is observed in the reciprocal space maps, as is expected for a material with multiple ferroic orders near a phase boundary.

Figure S8

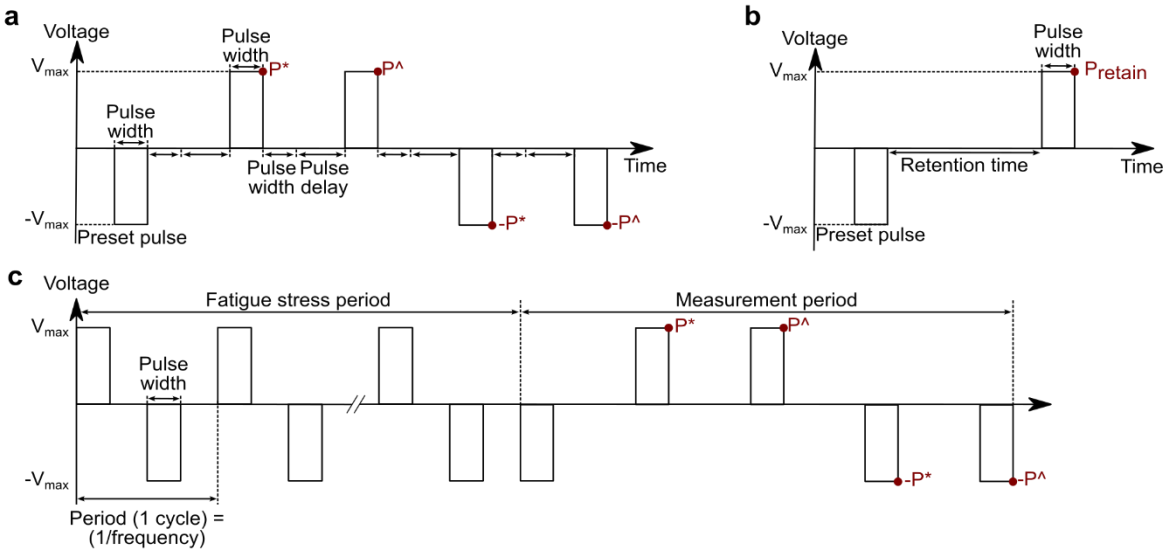

Figure S8. Pulse sequences of electrical measurements. Pulse sequences for the (a) PUND, (b) retention, and (c) fatigue measurements. For PUND and fatigue measurements, both the switched polarization (P*) and unswitched polarization (P^) polarizations were measured, from which the remnant polarization can be calculated: $2P_{remnant} = P^* - P^\wedge$.

Figure S9

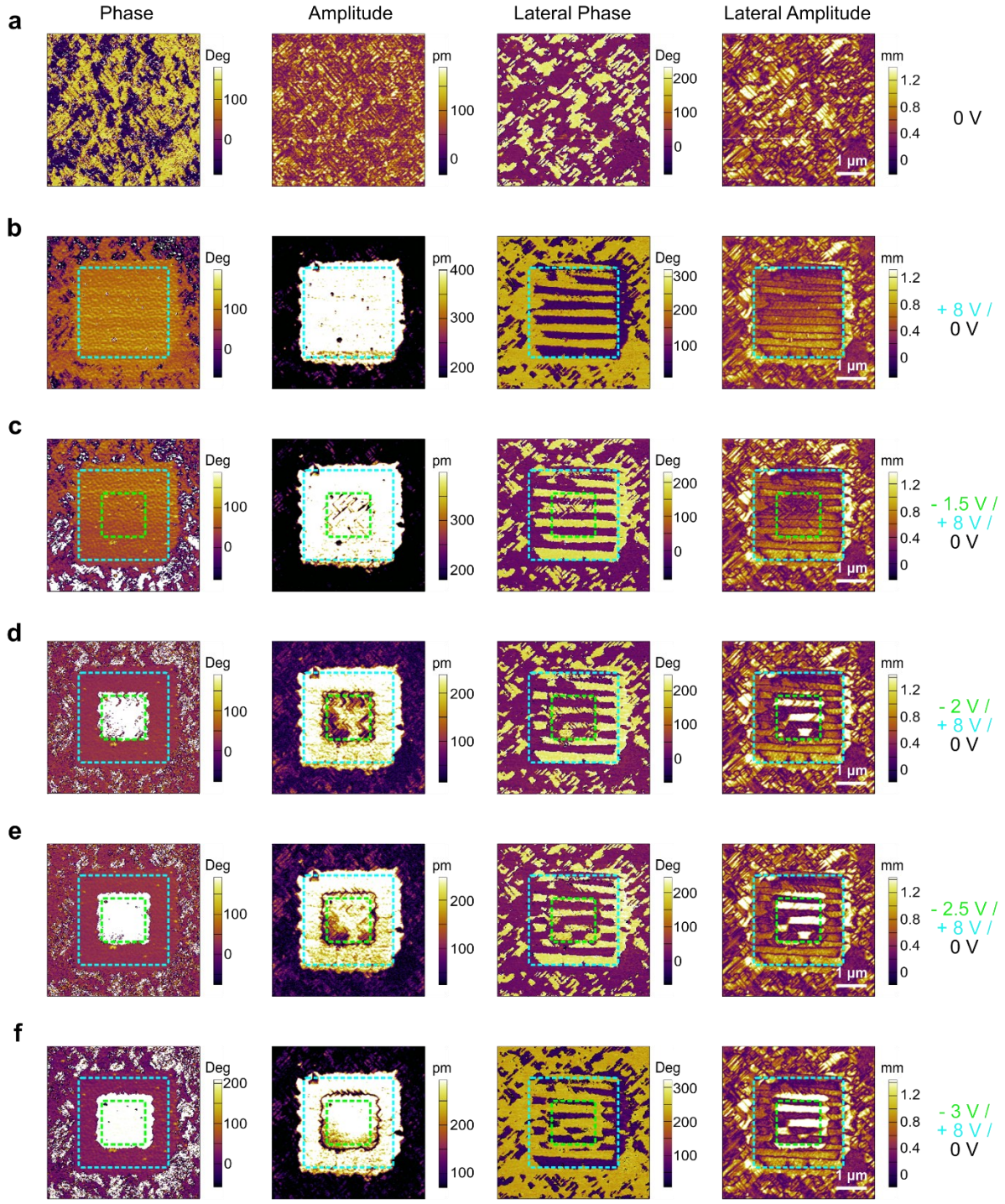

Figure S9. Piezoresponse force microscopy of 100 nm $NaNbO_3$ switching. Vertical phase, vertical amplitude, lateral phase, and lateral amplitude piezoresponse force microscopy (PFM) images taken after box-in-box poling of a $NaNbO_3$ / $La_{0.7}Sr_{0.3}MnO_3$ / $SrTiO_3$ heterostructures with 100 nm $NaNbO_3$. +8 V was first applied (b) to a 3 x 3 μm^2 area (blue), with subsequent increasing negative voltages applied (c-f) to an inner 1.5 x 1.5 μm^2 area (green).

Figure S10

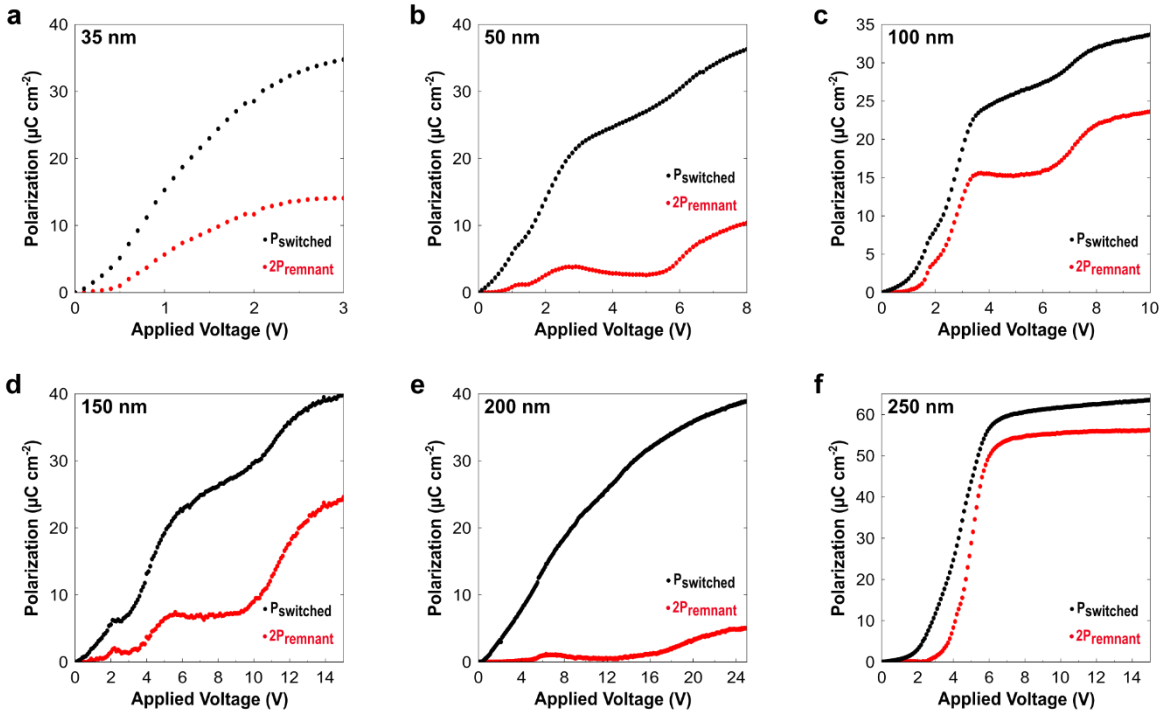

Figure S10. Thickness dependence of PUND. Evolution of switched polarization and remnant polarization from PUND measurements as a function of applied voltage with a 1ms pulse width for (a) 35, (b) 50, (c) 100, (d) 150, (e) 200, and (f) 250 nm thick $NaNbO_3$.

Figure S11

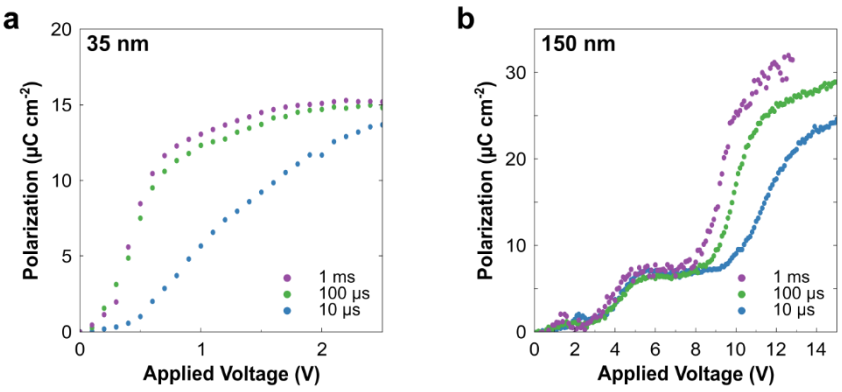

Figure S11. Pulse width dependence of PUND. PUND measurements of the remnant polarization as a function of applied voltage for (a) 35 and (b) 150 nm thick $NaNbO_3$ with varying pulse widths.

Figure S12

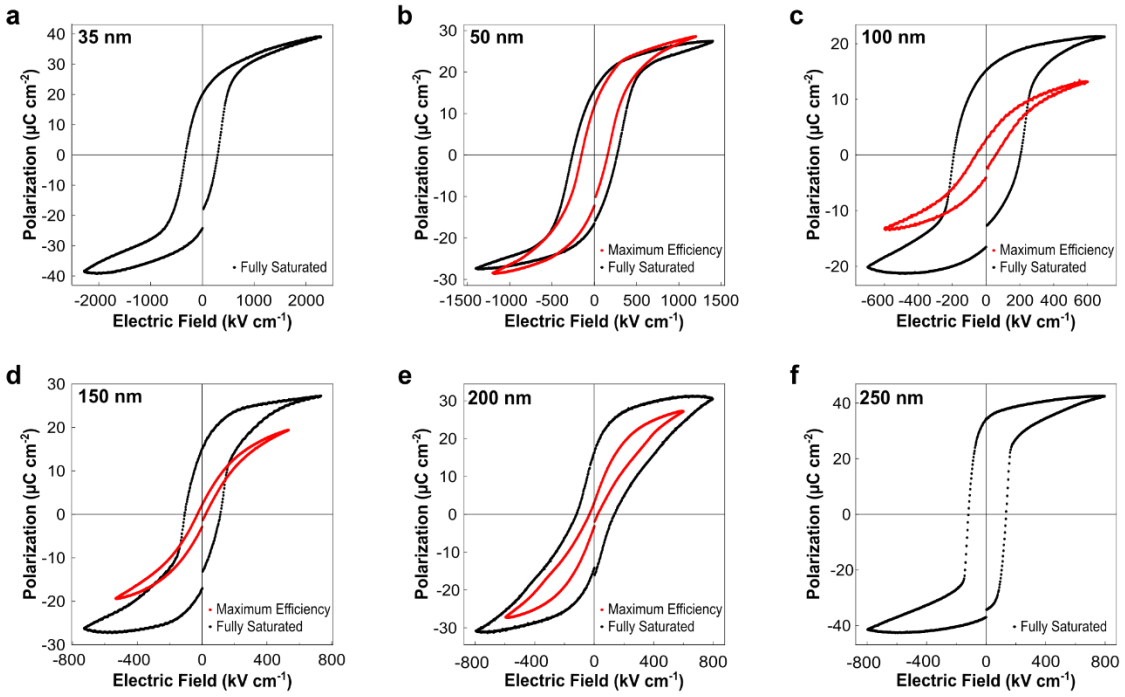

Figure S12. Variation of ferroelectric hysteresis for maximum efficiency. Polarization – electric field measurements at 1 kHz for (black) full switching, with the applied field necessary for complete saturation, and (red) the applied field achieving highest efficiency at the given thickness with $NaNbO_3$ thicknessess of (a) 35 nm, (b) 50 nm, (c) 100 nm, (d) 150 nm, (e) 200 nm, and (f) 250 nm.

Figure S13

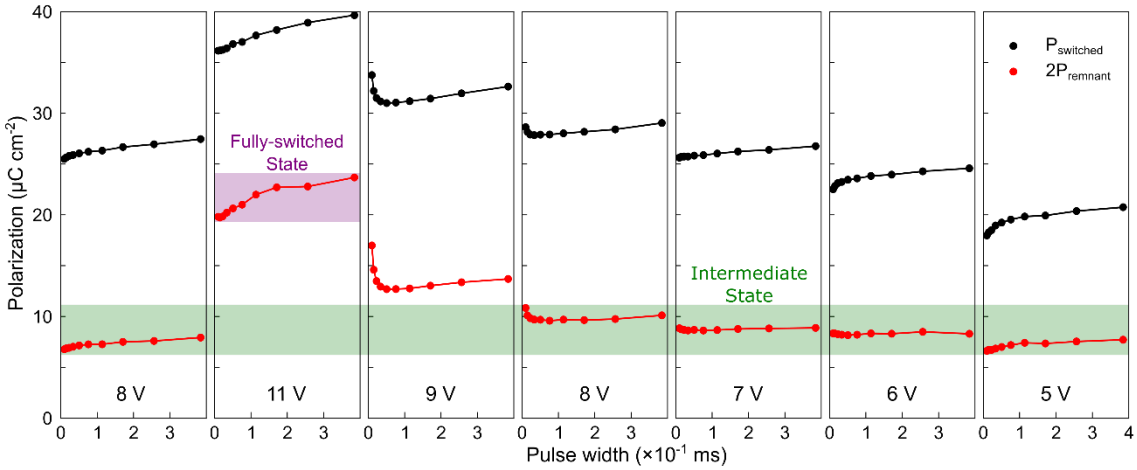

Figure S13. Reversibility of multiple polarization states in PUND measurements in 150 nm $NaNbO_3$. Successive PUND measurements (pulse sequence in Figure S8) were performed with varying voltage (in the left-to-right order shown in the figure), with steadily increasing pulse width utilized at each voltage. Both the switched and remnant polarizations indicate a return to the intermediate state upon application of an intermediate voltage (5-8 V) even after the sample is poled to the fully-switched state (11 V).

Figure S14

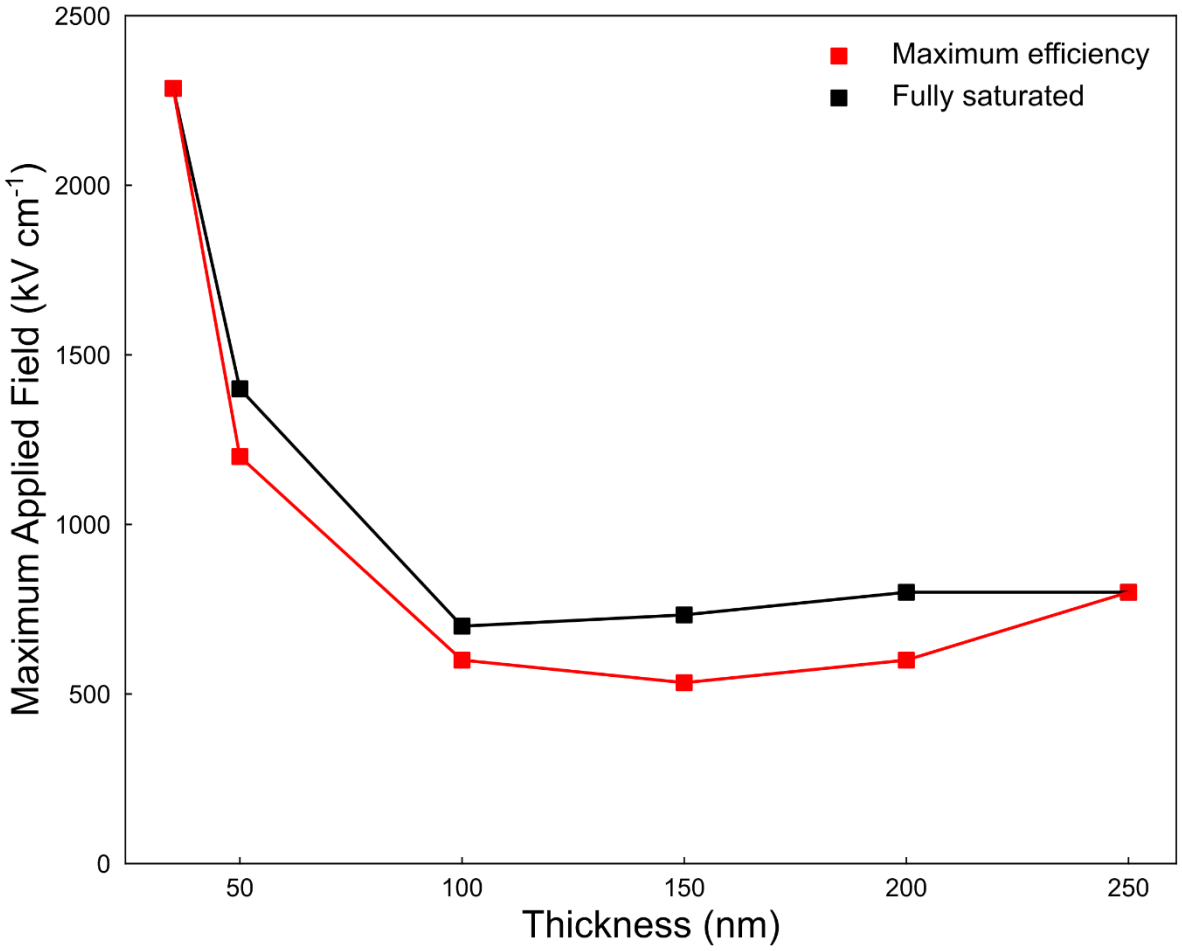

Figure S14. Required maximum applied electric fields for full saturation and maximum efficiency corresponding to the reported loops in Figure S11 at 1 kHz. (black) Fully switched loops with the field required to reach full saturation and (red) loops with highest efficiency at that thickness, including intermediate switching states.

Figure S15

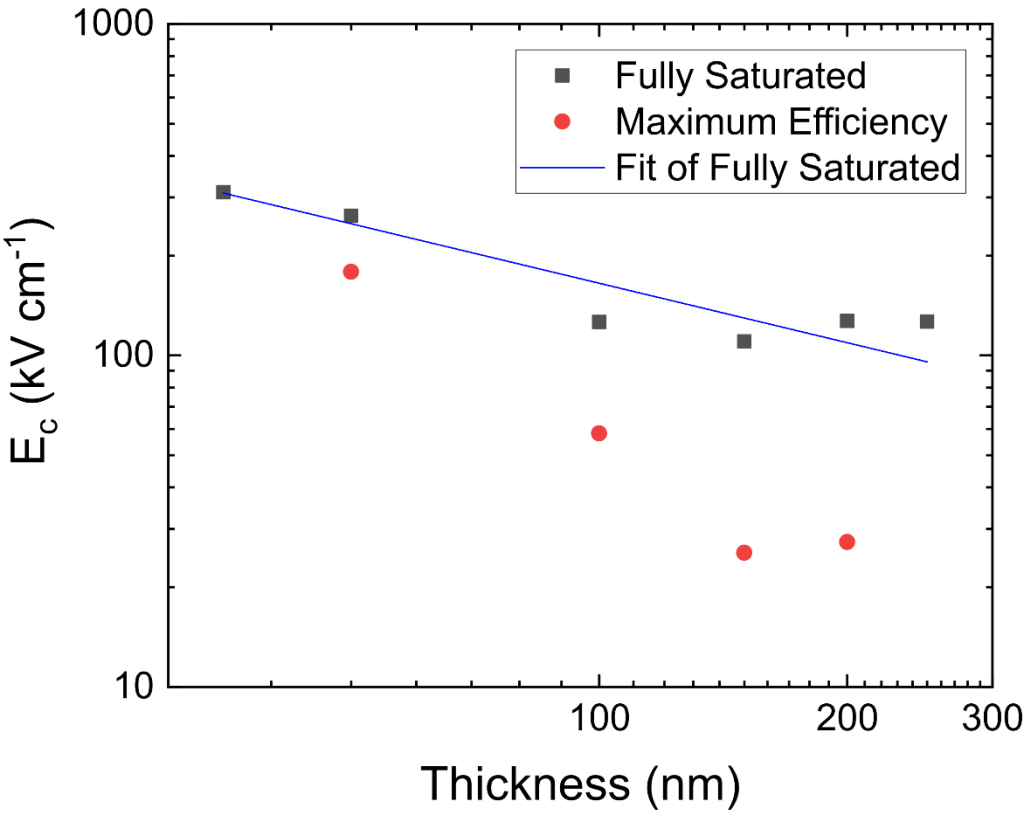

Figure S15. Deviation from Janovec-Kay-Dunn-like behavior for maximum efficiency loops. Coercive field as a function of thickness for the fully saturated and maximum efficiency hysteresis loops from Figure S11. The fully saturated loops closely follow Janovec-Kay-Dunn-like scaling, with a power law (y = a*x^b) fit yielding parameters of a = 2571.17172 ± 1044.04016 and b = -0.59604 ± 0.09867. The predicted exponent of -2/3 from the semi-empirical scaling relationship is within the error bounds. When operating at lower maximum applied fields to achieve maximum efficiency, the coercive field no longer follows the same scaling relationship.

Figure S16

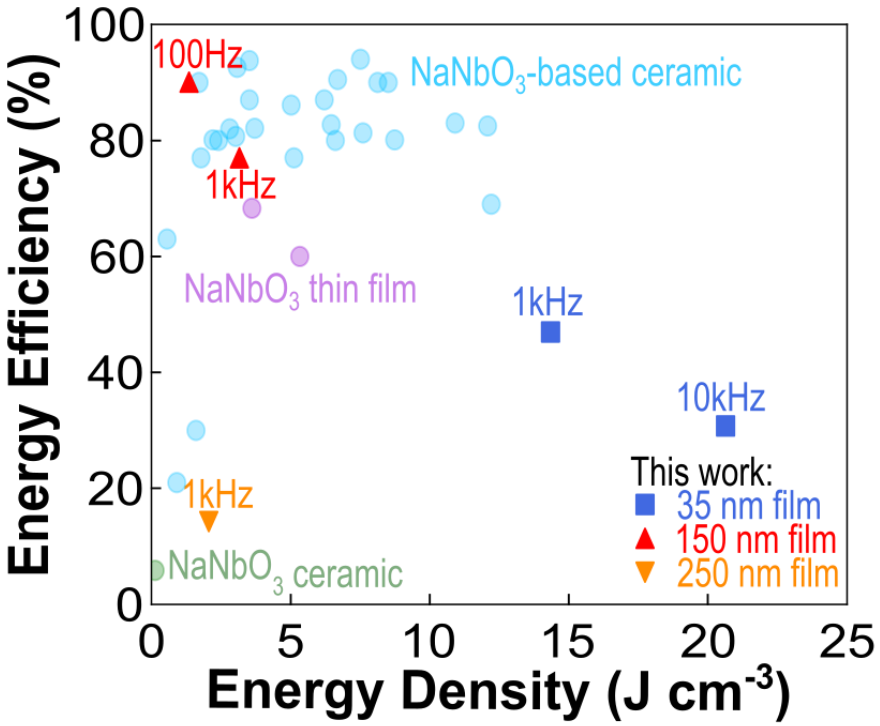

Figure S16. Comparison of energy storage parameters with $NaNbO_3$-based ceramics. Energy storage properties of various $NaNbO_3$-based systems, including this work as well as literature reports of pure ceramic $NaNbO_3$ (green), $NaNbO_3$-based ceramic compositions (light blue), and other $NaNbO_3$ and $NaNbO_3$-based thin films (purple) (data provided in Table S1). The intermediate state enables efficiencies comparable chemically-doped ceramics while the thinnest 35 nm film exceeds any previously reported energy storage densities for $NaNbO_3$-based systems.

Table S1. Energy storage parameters of $NaNbO_3$ and $NaNbO_3$-based materials from previous reports in literature with accompanying references.

Reference	Composition	Sample Geometry	Energy Density [J cm^{-3}]	Energy Efficiency [%]
M.-H. Zhang et al. (2023) [30]	$NaNbO_3$	Bulk	0.12	5
H. Qi et al. (2019)[51]	$0.76NaNbO_3 – 0.24(Bi_{0.5}Na_{0.5})TiO_3$	Bulk	12.2	69
M.-H. Zhang et al. (2023)[30]	$0.95NaNbO_3 – 0.05SrSnO_3$	Bulk	0.9	21
M.-H. Zhang et al. (2023)[30]	$0.91NaNbO_3 – 0.09SrSnO_3$ + 1% wt. MnO_2	Bulk	1.7	90
Z. Chen et al. (2022) [52]	$0.5NaNbO_3 – 0.5NaTaO_3$	Bulk	2.2	80.1
Z. Liu et al. (2018) [53]	$0.96NaNbO_3 – 0.04CaZrO_3$	Bulk	0.55	63
A. Xie et al. (2022) [54]	$0.84NaNbO_3 – 0.16CaTiO_3$	Bulk	6.6	80
A. Xie et al. (2022) [54]	$0.82NaNbO_3 – 0.18CaTiO_3$	Bulk	6.2	87
H. Qi et al. (2020) [55]	$0.57BiFeO_3 – 0.33BaTiO_3 – 0.1NaNbO_3$ + 0.1% wt. MnO_3 + 0.2% wt $BaCu(B_2O_5)$	Bulk	8.12	90
J. Lei et al. (2024) [56]	$0.82NaNbO_3 – 0.1BaZrO_3 – 0.08Bi(Mg_{0.5}Ti_{0.5})O_3$	Bulk	7.5	94
S. Zhang et al. (2024) [57]	$0.8NaNbO_3 – 0.2Bi(Ni_{0.5}Hf_{0.5})O_3$	Bulk	6.45	82.72
C. Sun et al. (2021) [58]	$0.78NaNbO_3 – 0.22Ba(Mg_{1/3}Nb_{2/3})O_3$	Bulk	3.51	87
H. Qi et al. (2019) [59]	$0.9NaNbO_3 – 0.06BaZrO_3 – 0.04CaZrO_3$	Bulk	1.59	30
J. Jiang et al. (2021) [60]	$(Na_{0.91}Bi_{0.09})(Nb_{0.94}Mg_{0.06})O_3$	Bulk	10.9	83
S. Zhang et al. (2023) [61]	$0.8NaNbO_3 – 0.2Bi(Mg_{0.5}Hf_{0.5})O_3$	Bulk	3.51	93.77
A. Xie et al. (2024) [62]	$0.68NaNbO_3 – 0.32(Bi_{0.5}Li_{0.5})(Zr_{0.4}Ti_{0.6})O_3$	Bulk	8.5	90
A. Xie et al. (2021) [63]	$0.68NaNbO_3 – 0.32(Bi_{0.5}Li_{0.5})TiO_3$	Bulk	8.73	80.1
J. Ye et al. (2019) [64]	$0.9NaNbO_3 – 0.1Bi(Mg_{2/3}Nb_{1/3})O_3$	Bulk	2.8	82
J. Ye et al. (2019) [64]	$0.85NaNbO_3 – 0.15Bi(Mg_{2/3}Nb_{1/3})O_3$	Bulk	2.4	80
W. Yang et al. (2022) [65]	$Na_{0.7}Bi_{0.1}Nb_{0.9}Ta_{0.1}O_3$	Bulk	6.68	90.5
J. Wang et al. (2021) [66]	$0.95NaNbO_3 – 0.05La(Mn_{0.5}Ni_{0.5})O_3$	Bulk	1.77	77
J. Shi et al. (2020) [67]	$0.78NaNbO_3 – 0.22Bi(Mg_{2/3}Ta_{1/3})O_3$	Bulk	5.01	86.1
M. Zhou et al. (2018) [68]	$0.8NaNbO_3 – 0.2SrTiO_3$	Bulk	3.02	80.7

J. Ma et al. (2022) [69]	$0.88NaNbO_3$ – $0.12(Bi_{0.9}Na_{0.1})(Fe_{0.8}Ti_{0.2})O_3$	Bulk	12.07	82.5
R. Zhao et al. (2024) [70]	$0.85NaNbO_3$ – $0.15Bi(Mg_{0.2}Hf_{0.2}Ni_{0.2}Zn_{0.2}Ta_{0.2})O_3$	Bulk	5.11	77
L.-F. Zhu et al. (2021) [71]	$0.8NaNbO_3$ – $0.04CaZrO_3$ – $0.16Bi_{0.5}Na_{0.5}TiO_3$	Bulk	3.7	82.1
P. Zhao et al. (2022) [72]	$0.6BaTiO_3$ – $0.4NaNbO_3$	Bulk	3.07	92.6
H. Dong et al. (2022) [25]	$Na_{0.9}NbO_3$	Thin Film	5.32	60
Y. Zhang et al. (2024) [73]	$NaNbO_3$	Thin Film	3.6	68.31